Observation Impacts on the Mid-Atlantic Bight Front and Cross-Shelf Transport in 4D-Var Ocean State Estimates: Part I – Multiplatform Analysis

by

Julia Levin (julia@marine.rutgers.edu)[a], Hernan G. Arango (arango@marine.rutgers.edu)[a], Bruce Laughlin (blaughli@ucsc.edu)[b], Elias Hunter (hunter@marine.rutgers.edu)[a], John Wilkin (wilkin@marine.rutgers.edu)[a] and Andrew M. Moore (ammoore@ucsc.edu)[b*]

a: Department of Marine and Coastal Sciences, Rutgers, The State University of New Jersey, 71 Dudley Road, New Brunswick NJ 08901.
b: Department of Ocean Sciences, University of California, 1156 High Street, Santa Cruz CA 95062.

* Corresponding author: ammoore@ucsc.edu
Department of Ocean Sciences, University of California, 1156 High Street, Santa Cruz CA 95062

Abstract

A nested configuration of the Regional Ocean Modeling System (ROMS) comprising three grids was used in conjunction with a 4-dimensional variational (4D-Var) data assimilation system to compute ocean state estimates of the Mid-Atlantic Bight (MAB). The three nested grids have a horizontal resolution ranging from ~7 km to ~0.8 km and capture circulation regimes that span the Gulf Stream western boundary current, through the mesoscale eddy field, and down to the rapidly evolving and energetic sub-mesoscale. All of these circulation regimes are challenging for any data assimilation system, yet the 4D-Var system was found to perform well across this range of space- and time-scales. The observational data used to constrain the ocean state estimates comes from a wide range of remote sensing, *in situ*, and mobile platforms. An adjoint-based procedure was used to compute the impact of each observing platform on several different indexes that describe the position of the MAB front, stratification, and associated cross-shelf exchange processes in the vicinity of the U.S. National Science Foundation's Ocean Observatories Initiative Pioneer Array. The impact of observations from each observing platform on the chosen indexes varies across the three grids. It is a function of several factors that include the nature of the background circulation and the level of error assumed for the background ocean state and the observations. The geographic distribution of the observation impacts is remarkably robust across the various indexes and the three grids. In addition, observations that are both local to and remote from the target regions that define each index can exert a significant influence on the circulation. Variations in the observation impacts through time can be used to identify observations that exert unexpectedly large influence on the 4D-Var analyses (*i.e.*, outliers), and routine monitoring of observation impacts is a useful indicator of the efficacy of different components of the observing system. Also, the observation impacts were found to be a useful performance indicator for the data assimilation system.

Keywords: Data assimilation; 4D-Var; observation impacts; Mid-Atlantic Bight; Pioneer Array

1 Introduction

Data assimilation is an integral component of any ocean analysis and forecast system. It is now a mainstream activity at most operational numerical weather prediction centers and many research institutions, both on regional and global scales (Moore *et al.*, 2019). Ocean data streams are dominated by remote sensing instruments that observe temperature and sea level, but developments in novel sensors and autonomous platforms are rapidly expanding the delivery of *in situ* observations. Though typically inhomogenous in space and time sampling, and much less numerous, subsurface *in situ* data are an invaluable complement to dense satellite observations. When assimilated into forecast models, the information that these various platforms provide can interact in complex and sometimes surprising ways, and data from one platform can support measurements from another. Unraveling the influence of the respective observations on the ensuing ocean analyses and forecasts can be very challenging. Nevertheless, given the considerable financial and human resources required to deploy and maintain ocean observing networks, the routine quantitative assessment of the impact of observations on analysis-forecast systems is an important activity. Indeed, observation impact assessments now form a critical component of most operational numerical weather prediction systems.

The focus of this study is the impact of observations in an analysis-forecast system based on the Regional Ocean Modeling System (ROMS) that encompasses the Mid-Atlantic Bight (MAB) and Gulf of Maine (GoM) in the NW Atlantic (Fig. 1a) and is run in near real-time in support of the U.S. Integrated Ocean Observing System (IOOS) Mid-Atlantic Regional Association Coastal Ocean Observing System (MARACOOS). A prominant feature of the MAB region is a shelf-break front separating the warm, saline waters of the subtropical gyre from the cooler, fresher waters of the continental shelf (Mountain, 2003). Intrinsic instabilities of the front (Fratantoni and Pickart, 2003) and eddy-shelf interactions tied to Gulf Stream induced warm core rings (Zhang and Gawarkiewicz, 2015) contribute to the complexity of MAB shelf-break dynamics (Gawarkiewicz *et al.*, 2018) and are a major focus of the U.S. National Science Foundation's (NSF) Ocean Observatories Initiative (OOI). As part of this initiative, the Pioneer Array, comprising fixed moorings and a fleet of automomous underwater vehicles is deployed at the continental shelf-break (Figs. 1b,c) with a majority of the instruments operational since April 2014. The primary aim of Pioneer is to increase understanding of the processes responsible for the transport of water masses across the shelf-break, and their relationship to forcing on a range of time scales, but its limited-area, high-density sampling pattern provides a valuable supplement to the wider-scope MARACOOS observing system and presents exceptional opportunites to methodically contrast the impact of such disparate observing system designs.

There have been several efforts in oceanography to quantify the impact of observing systems on ocean analyses using a variety of methods that include: observing system experiments (*e.g.*, Balmaseda *et al.*, 2007; Oke and Schiller, 2007; Smith and Haines, 2009); spectral analysis of the representer matrix (Le Hénaff *et al.*, 2009); quantification of the degrees of freedom of the observing system (Moore *et al.*, 2011b); assessment of observation footprints (Oke and Sakov, 2012); and ensemble methods (Storto *et al.*, 2013). Extensive reviews of these efforts can be found in Oke *et al.* (2015a,b) and Fujii *et al.* (2019). The present study uses an adjoint-based approach developed by Langland and Baker (2004) and builds on the work of Moore *et al.* (2017) and Levin *et al.* (2019).

The goal of this study is to quantify the impact of the various components of the MARACOOS observing system on circulation estimates derived from the ROMS 4-dimensional variational (4D-Var) data assimilation system. In light of the goals of the NSF OOI Pioneer Array, a specific focus is the extent to which the observing system can inform ROMS about shelf-break exchange processes in the vicinity of the MAB front. A brief overview of the 4D-Var and observation impact methodology employed is given in section 2, although the reader is directed to Levin *et al.* (2019) for a more detailed and thorough description. Section 3 describes the configuration of ROMS and 4D-Var, the various data sources used, and documents the performance of the data assimilation system. The observation impacts are quantified in terms of specific indexes that target different aspects of the shelf-break circulation, and these are introduced in section 4. Section 5 presents a summary of the impact of the observations from the various components of the observing system on the suite of circulation indexes identified, while sections 6 and 7 focus specifically on the remote sensing and *in situ* observations, respectively. A summary and conclusions follow in section 8. The companion study of Levin *et al.* (2020; hereafter referred to as Part II) presents a detailed analysis of the impact of the observations from the Pioneer Array.

2 Observation Impacts and 4D-Var

The methodology used in ROMS to compute the impact of the observations on 4D-Var ocean circulation estimates is based on that employed in numerical weather prediction originally developed by Langland and Baker (2004; hereafter LB). The procedure used in ROMS is described in detail by Moore *et al.* (2011ab, 2017). Levin *et al.* (2019; hereafter, L19) have explored in detail the impact of remote sensing observations in one component of the ROMS configuration considered here, so for brevity, only a short overview of the approach will be presented.

In the sequel, the ROMS state-vector will be denoted by $\boldsymbol{x}$ and comprises all of the ocean grid-point values of the ROMS prognostic variables, namely temperature (*T*), salinity (*S*), two components of horizontal velocity (u,v) and free-surface height (ζ). If $\boldsymbol{x}^b$ denotes the background state-vector and $\boldsymbol{x}^a$ is the analysis, then:

$$\boldsymbol{x}^a = \boldsymbol{x}^b + \boldsymbol{K}\left(\boldsymbol{y}^o - H(\boldsymbol{x}^b)\right) \tag{1}$$

where $\boldsymbol{y}^o$ denotes the vector of observations, H is the observation operator that maps from state-space to observation-space, and $\boldsymbol{K}$ is the Kalman gain matrix. In the case of 4D-Var, the observation operator H includes the nonlinear model. In the ROMS application considered here, the dual form of 4D-Var was used, in which case $\boldsymbol{K} = \boldsymbol{B}\boldsymbol{H}^T(\boldsymbol{H}\boldsymbol{B}\boldsymbol{H}^T + \boldsymbol{R})^{-1}$ where $\boldsymbol{B}$ and $\boldsymbol{R}$ are background error and observation error covariance matrices respectively, and $\boldsymbol{H}$ represents the tangent linearization of the observation operator H. In 4D-Var, $\boldsymbol{H}$ includes the tangent linearization of the nonlinear model and $\boldsymbol{H}^T$ includes the adjoint model.

The analysis $\boldsymbol{x}^a$ is identified by minimizing the incremental formulation of the 4D-Var cost function (Courtier *et al.*, 1994). Specifically, the Lanczos formulation of the Restricted **B**-

Preconditioned Conjugate Gradient (RPCG) method is used (Gratton and Tshimanga, 2009) as described by Gürol *et al.* (2014). Following this approach, the dual Kalman gain matrix for each outer-loop is factorized according to $\widetilde{\boldsymbol{K}} = \boldsymbol{B}\boldsymbol{H}^T\boldsymbol{V}_m\boldsymbol{T}_m^{-1}\boldsymbol{V}_m^T\boldsymbol{H}\boldsymbol{B}\boldsymbol{H}^T\boldsymbol{R}^{-1}$ where m is the number of inner-loops, and each of the m-columns of $\boldsymbol{V}_m$ represents each CG descent direction normalized to unit amplitude (the so-called Lanczos vectors), and $\boldsymbol{T}_m$ is a known tridiagonal matrix. In this form, $\widetilde{\boldsymbol{K}}$ represents a reduced dimension approximation of $\boldsymbol{K}$.

The impact of the observations on the analysis $\boldsymbol{x}^a$ can be quantified in terms of their influence on a chosen index, $I(\boldsymbol{x})$. Specifically, $\Delta I = I(\boldsymbol{x}^a) - I(\boldsymbol{x}^b)$ represents the change in I due to assimilating the observations $\boldsymbol{y}^o$, and following LB can be expressed to 1st-order as $\Delta I \approx \left(\boldsymbol{y}^o - H(\boldsymbol{x}^b)\right)^T \boldsymbol{K}^T(\partial I/\partial \boldsymbol{x})|_{\boldsymbol{x}^b}$. The reduced dimension approximation $\widetilde{\boldsymbol{K}}$ of $\boldsymbol{K}$ then leads to:

$$\Delta I \approx \left(\boldsymbol{y}^o - H(\boldsymbol{x}^b)\right)^T \boldsymbol{R}^{-1}\boldsymbol{H}\boldsymbol{B}\boldsymbol{H}^T\boldsymbol{V}_m\boldsymbol{T}_m^{-1}\boldsymbol{V}_m^T\boldsymbol{H}\boldsymbol{B}(\partial I/\partial \boldsymbol{x})|_{\boldsymbol{x}^b} \qquad (2)$$

where $(\partial I/\partial \boldsymbol{x})|_{\boldsymbol{x}^b}$ represents the derivative of I with respect to $\boldsymbol{x}$ evaluated using the background $\boldsymbol{x}^b$. From (2), it is clear that ΔI is given by the dot-product of the innovation vector $\boldsymbol{d} = \left(\boldsymbol{y}^o - H(\boldsymbol{x}^b)\right)$ and the vector $\boldsymbol{g} = \boldsymbol{R}^{-1}\boldsymbol{H}\boldsymbol{B}\boldsymbol{H}^T\boldsymbol{V}_m\boldsymbol{T}_m^{-1}\boldsymbol{V}_m^T\boldsymbol{H}\boldsymbol{B}(\partial I/\partial \boldsymbol{x})|_{\boldsymbol{x}^b}$, which quantifies the impact of the observations on ΔI. Since each element of $\boldsymbol{d}$ is uniquely associated with a single observation, so then are the corresponding elements of $\boldsymbol{g}$ such that the product $d_i g_i$ represents the contribution (aka impact) of the i^{th} observation to ΔI. The observation impacts for a particular data assimilation cycle can, therefore, be easily computed from the archived 4D-Var Lanczos vectors.

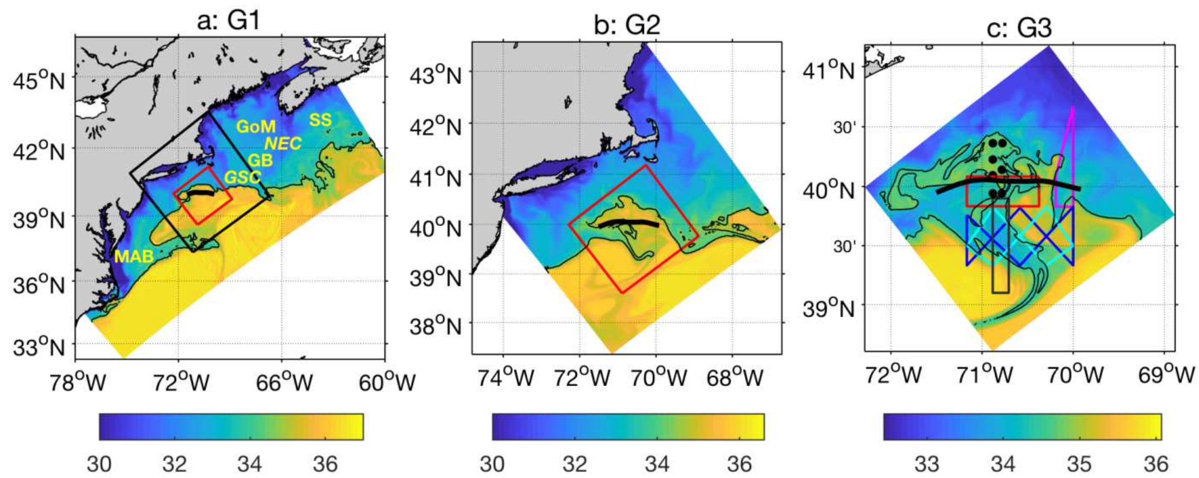

Figure 1: Snapshots of the sea surface salinity on 16 May 2014 from 4D-Var analyses on the three nested grids denoted (a) G1, (b) G2, and (c) G3. The 34.5 isohaline is often used as a proxy for the position of the Mid-Atlantic Bight shelf-break front and is highlighted in black in each figure. The location and extent of grids G2 (black rectangle) and G3 (red rectangle) are shown superimposed on G1 in (a). Also shown in (c) are the locations of the Pioneer moorings array (black dots), and the nominal Pioneer glider array (colored lined). The solid heavy black line in each panel indicates the target section that follows the 200m isobath used to quantify shelf exchange defined by

equations (6)-(10). The locations of geographical features mentioned in the main text are also shown in (a): GoM=Gulf of Maine, GB=Georges Bank, GSC=Great South Channel, MAB-Mid-Atlantic Bight, NEC=North East Channel, SS=Scotian Shelf.

3 Model Configuration and Data Assimilation

The ROMS configuration used here spans the Mid-Atlantic Bight and the Gulf of Maine, as illustrated in Fig. 1, and three layers of nesting were employed. The outer-most domain, G1, has a horizontal resolution ~7 km and 40 terrain-following levels stretched so that the thickness of the surface-most layers is in the range 0.1-1.8 m and 0.1-3.4 m near the bottom over the continental shelf. The choice of number of vertical levels was based on previous experience with ROMS in the NE Atlantic (*e.g.* Fennel et al, 2006; Zhang et al, 2010; Wilkin and Hunter, 2013). The middle refined grid, G2, is centered on the NSF OOI Pioneer Array with a horizontal resolution of ~2.4 km, also with 40 terrain-following levels in the vertical. The innermost refined grid, G3, is likewise centered on the Pioneer Array with 40 levels in the vertical and ~0.8 km horizontal resolution. G1 was constrained at the open boundaries using data from the Mercator-Océan global analysis (Drévillon *et al.*, 2008) with temperature and salinity adjusted to remove seasonal bias compared to a local, regional climatology of Fleming (2016).

Type & platform	**Source**	**Sampling rate and resolution**	**Super-obs averaging[1]**			**Obs error**
			G1	**G2**	**G3**	
AVHRR IR SST	MARACOOS.org & NOAA Coastwatch	4 passes per day, 1 km	3 h	3 h	3 h	σ_b
GOES IR SST	NOAA Coastwatch	Hourly, 6 km	3 h	3 h	3 h	$2\sigma_b$
AMSR2, TRMM and WindSat microwave SST	NASA JPL PO.DAAC	Daily, 15 km	3 h	3 h	3 h	$1.25\sigma_b$
SSH Jason, AltiKa, CryoSat	RADS, TU Delft	~1 pass daily, ~7 km				0.04 m
in situ T, S: NDBC buoys, Argo floats, XBT, surface drifters	Met Office En4.2	Variable[2]	Std.lev[2]	Std.lev[2]	Std.lev[2]	$0.25\sigma_b\sigma_o/\sigma_{max}$[3]
Surface velocity: HF-radar	MARACOOS.org	Hourly, 6 km	24 km	24 km	24 km	$0.5\sigma_b$
in situ T,S: MARACOOS gliders	IOOS Glider DAC	Variable[2]	2 h, Std.lev[2]	1 h, Std.lev[2]	0.33 h, Std.lev[2]	$0.25\sigma_b\sigma_o/\sigma_{max}$[3]
in situ T,S: Gulf of Maine	NERACOOS.org[4]	Hourly, 10 buoys				σ_b
in situ u,v: Gulf of Maine		Hourly, 9 buoys[1]				$0.5\sigma_b$
in situ T,S: Pioneer moorings	NSF Ocean Observatories Initiative[7]	~3 h profiles, 7 moorings[5] ~60% data availability[6]	2 h, Std.lev[2]	1 h, Std.lev[2]	0.33 h, Std.lev[2]	$0.25\sigma_b\sigma_o/\sigma_{max}$[3]
in situ T,S: Pioneer gliders		Variable[2] ~4 h, ~4 km	2h, Std.lev[2]	1h, Std.lev[2]	0.33 h, Std.lev[2]	$0.25\sigma_b\sigma_o/\sigma_{max}$[3]

in situ u,v: Pioneer moorings		30 min, ~75% data availability[6]	Std.lev[2]	Std.lev[2]	Std.lev[2]	$0.5\sigma_b$

Table 1: A summary of the observational data assimilated into ROMS during 2014–2017, the procedure for forming super observations, and the observation errors assigned to each observation type. The final column, σ_o and σ_b denote the standard deviation of observation errors and background errors respectively, the formulae given are the scaling relationships used for the indicated observation types. The superscripts provide additional information. 1: All data that were sampled at a horizontal resolution higher than that of the model were formed into super observations at the resolution of the ROMS grid unless otherwise indicated. 2: Profile data were binned in the vertical using the WOD atlas standard depths (Boyer *et al.*, 2009). 3: Here σ is the standard deviation of all observations that fall within a vertical bin (see comment 1) and σ_{max} is the maximum value of all σ in a vertical profile. 4: NERACOOS = North East Regional Association Coastal Ocean Observing System. 5: Moorings 2 and 4 deployed November 2017. 6: Average over 2014-2017. 7: Data downloaded from NSF OOI Data Portal http://ooinet.oceanobservatories.org and aggregated by platform at http://www.myroms.org:8080/erddap/info

In typical forward simulations, all three grids can be run using one- or two-way nesting. The open boundary Mean Dynamic Topography (MDT) and seasonal cycle of sea surface height (SSH) variation were also adjusted for bias using a regional, data assimilative, climatological, seasonal analysis computed following the procedure described by Levin *et al.* (2018) and Wilkin *et al.* (2018). The sub-tidal mesoscale variability captured by Mercator-Océan is retained. Harmonic tidal forcing (Mukai *et al.*, 2002) was added to the boundary SSH and depth-averaged velocity data. Sea surface wind stress and heat and freshwater fluxes were derived from 3-hourly National Centers for Environmental Prediction (NCEP) North American Mesoscale (NAM) forecast marine boundary layer conditions and standard bulk formulae of Fairall *et al.* (2003). NAM air pressure was also imposed as a surface condition to the pressure gradient force so that the model computes a dynamic Inverted Barometer (IB) response. Accordingly, an equilibrium IB sea level term is added to the open boundary sea level data, which is standard practice in altimeter data processing. Daily river in-flows were imposed at 22 discharge sites based on U.S. Geological Survey and Water Survey of Canada observations and a statistical model that adjusts for ungauged portions of the watershed (Lopez *et al.* 2020, Wilkin *et al.* 2018).

A full description of the 4D-Var system applied to G1 can be found in Levin *et al.* (2018), Wilkin *et al.* (2018), and L19, so only a summary of the crucial points will be presented here. The data assimilation system used is the dual formulation of the ROMS 4-dimensional variational (4D-Var) system (Moore *et al.*, 2011a; Gürol *et al.*, 2014). ROMS 4D-Var was run using two outer-loops and seven inner-loops. A list of the data assimilated, and the source of each data type is given in Table 1 and span the period Jan 2014 - Dec 2017. The ROMS 4D-Var systems do not yet function across one- or two-way nested configurations, although this capability is currently under development. Therefore, the following strategy was employed to assimilate the available observations into the three grids: (1) Observations were first assimilated into G1 for the full 2014-2017 period using a 3-day assimilation window, and treating the model initial conditions, surface forcing (all components), and open boundary conditions as control variables. The analysis state $\boldsymbol{x}^a$ at the *end* of the previous 3-day 4D-Var cycle was used as the background state $\boldsymbol{x}^b$ at the *beginning* of the current analysis cycle. (2) Step (1) was then repeated for grid G2, using the 4D-Var analyses from each cycle of G1 as the background open boundary conditions for each 4D-Var cycle of G2. As in G1, the initial conditions, surface forcing (all components), and open boundary conditions were all adjusted during a 3-day 4D-Var cycle. (3)

Step (2) was then repeated for grid G3, using the 4D-Var analyses from each cycle of G2 as the background open boundary conditions for each 4D-Var cycle of G3. In this case, the 4D-Var window was reduced to 1-day, and only the initial conditions and open boundary conditions were adjusted during each 4D-Var cycle. Also, because of the considerable increase in computational expense, 4D-Var was only run on G3 for the period 2014-2015.

In combination, steps (1), (2) and (3) lead to corrections to the initial conditions every 3-days in the case of G1 and G2, and every day in the case of G3. In the case of G1 and G2, the surface fluxes are continuously adjusted during the 3-day assimilation cycle, while on G3 there are no corrections made to the surface forcing. On all three grids the open boundary conditions undergo continuous adjustments. Clearly, each child grid benefits from the 4D-Var estimate from the parent grid *only* at the child grid open boundaries. Therefore, each grid receives information from the observations only once, except for interior observation influences on the open boundary conditions. The background initial conditions for the *first* 4D-Var cycle on 1 Jan 2014 on G1 were taken from a previously computed 4D-Var reanalysis spanning the period 2007-2013 (see Wilkin *et al.*, 2018). The background initial conditions for the *first* cycle on 1 Jan 2014 on G2 and G3 were linearly interpolated from G1.

It is normal procedure to combine multiple observations of the same type that fall within a single grid cell and that are closely spaced in time into super observations. Super observations were computed where appropriate separately for each of the three grids (see Table 1). Therefore, given the difference in horizontal resolution of each grid, the observations assimilated into the model in each case within the overlapping region were not the same.

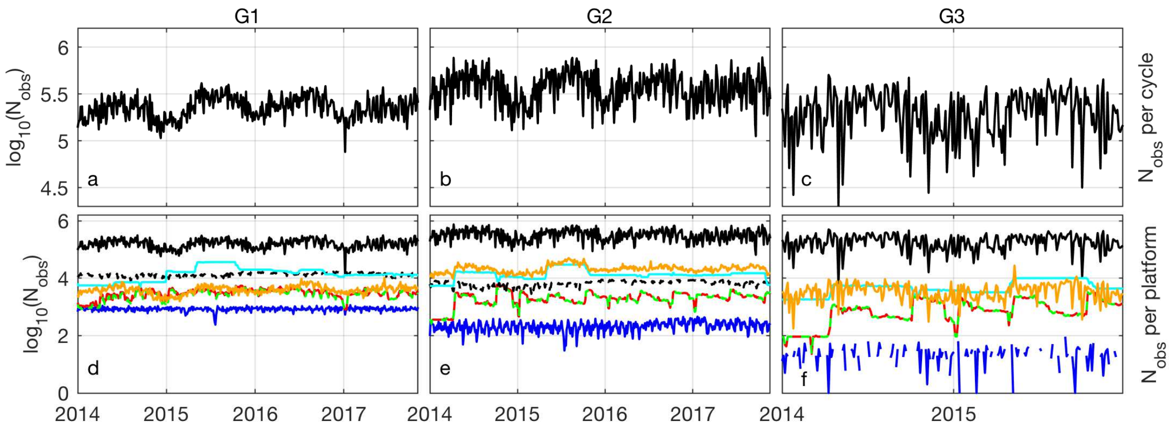

Figure 2: Time series of the $\log_{10}$ of the total number of observations from *all* platforms assimilated during each 4D-Var cycle on grid (a) G1, (b) G2, and (c) G3. Time series of the total of observations from each platform are also shown for (d) G1, (e) G2 and (f) G3: SST – solid black line; SSH – solid blue line; *in situ* temperature – solid red line; *in situ* salinity – green dashed line; gridded HF radar – black dashed line; *in situ* velocity – cyan line; total number of observations rejected – orange line. In the case of *in situ* instruments, the *total* number of observations that comprise all vertical profiles is shown.

Figure 2 shows time series of the *total* number of observations assimilated into the model on each grid during a 4D-Var cycle. Despite the changing size of the grid, and the shorter 4D-Var window length of G3, the total number of observations assimilated on each grid during each cycle is similar even though the grid resolution changes going from G1 to G2 to G3, because less "super-obing" is required on the higher resolution grids compared to G1. The Fig. 2 information can be readily converted to logarithm of the observation density by subtracting $\log_{10}$ of the number of grid points, which is 6.01, 6.25 and 6.45 for G1 though G3, respectively. This indicates that there is typically one observation per 10 grid cells in a 3-day cycle. Figure 2 also shows time series of the number of observations assimilated from each observing platform. Apart from satellite altimetry, the number of observations from each platform is similar across all three grids. On the other hand, for altimetry, there is an order of magnitude reduction in the number of observations going from one grid to the next due to the spatial separation of the altimeter ground tracks. Indeed, Fig. 2f shows that during some 4D-Var cycles, no altimeter tracks crossed G3.

As described in Moore *et al.* (2011a), the 4D-Var background error covariance $\boldsymbol{B}$ matrix was modeled following the diffusion operator approach of Weaver and Courtier (2001). The decorrelation length scales assumed in $\boldsymbol{B}$ for errors in each control variable are listed in Table 2, and these parameter choices are discussed in L19. All components of the surface fluxes were included in the control vector: both components of surface wind stress, the total surface heat flux, and the total surface freshwater flux. While formally the surface flux corrections should be computed every model time step, this is not practical, so the corrections were calculated every hour, and linearly interpolated in time. The standard deviations for the background surface errors were estimated from a multi-year run of the model without data assimilation.

The observation error covariance matrix $\boldsymbol{R}$ was assumed to be a diagonal matrix, and the observation errors are also summarized in Table 1 and discussed in L19. Quality control was also performed during each 4D-Var cycle following Andersson and Järvinen (1999), as described by Moore *et al.* (2013). Specifically, the innovation d_i associated with each observation is compared to the standard error based on the assumed standard deviations of the background (σ_b) and observation (σ_o) errors. In particular, if $d_i^2 > \alpha^2(\sigma_b^2 + \sigma_o^2)$, then the observation is rejected and not included in the analysis. The threshold parameter α is dependent on the type of observation and is given in Table 2 for the analyses on each grid considered here. A time series of the total number of observations rejected during each 3-day 4D-Var cycle is shown in Fig. 2 and is typically $O(10^3\text{-}10^4)$, indicating that only ~1% of the total number of observations were rejected based on the chosen criteria.

State variable	**Horizontal decorrelation scale (km) (G1|G2|G3)**	**Background quality control parameter α (G1|G2|G3)**
SSH	40 | 14 | 5	5 | 5 | ∞
Velocity	40 | 14 | 5	1.5 | 1.5 | ∞
Temperature	15 | 14 | 5	6 | 6 | 6
Salinity	15 | 14 | 5	12 | 12 | 12
Surface forcing	100 | 100 | -	-

Table 2: A summary of the decorrelation scales assumed for background errors in each control variable on all three grids. The vertical decorrelation length scale for all state variables of the initial conditions and open boundary conditions was chosen to be 10 m. In the case of the surface forcing, the same horizontal decorrelation lengths were imposed on all fields. The parameter α used for the background quality control rejection criteria is also indicated: $\alpha = \infty$ indicates that no background quality control check was applied to these data. A dash in any column indicates that the parameter is not applicable.

The performance of the 4D-Var system on G1 is described in detail by Levin *et al.* (2018), Wilkin *et al.* (2018), and L19. Figure 3 shows probability density functions (pdfs) for the innovations associated with observations of sea surface temperature (SST), SSH, *in situ* temperature, and *in situ* salinity for each grid. In principle, if $\boldsymbol{B}$ and $\boldsymbol{R}$ are correctly prescribed, the innovations $\boldsymbol{d}$ should be normally distributed with a covariance given by $(\boldsymbol{HBH}^T + \boldsymbol{R})$. Therefore, for reference, Fig. 3 also shows the pdfs for normal distributions with the same mean and standard deviation as the innovations computed during the 1st outer-loop. Clearly, for all observation types on all three grids, the innovation pdfs depart significantly from the expected normal distributions and are more reminiscent of a Laplacian distribution. For the most part, the mean innovations for temperature and salinity are close to zero for all three grids. The mean SSH innovations, however, are negative on all three grids, indicating that, on average, the mean model SSH exceeds that of the observations. For salinity, while the mean innovations are close to zero, there is an overall tendency for the model to favor negative innovations in all three grids, as evidenced by the skewed nature of the pdfs. The innovation pdfs for the 2nd outer-loop are qualitatively similar to those for the 1st outer-loop (not shown).

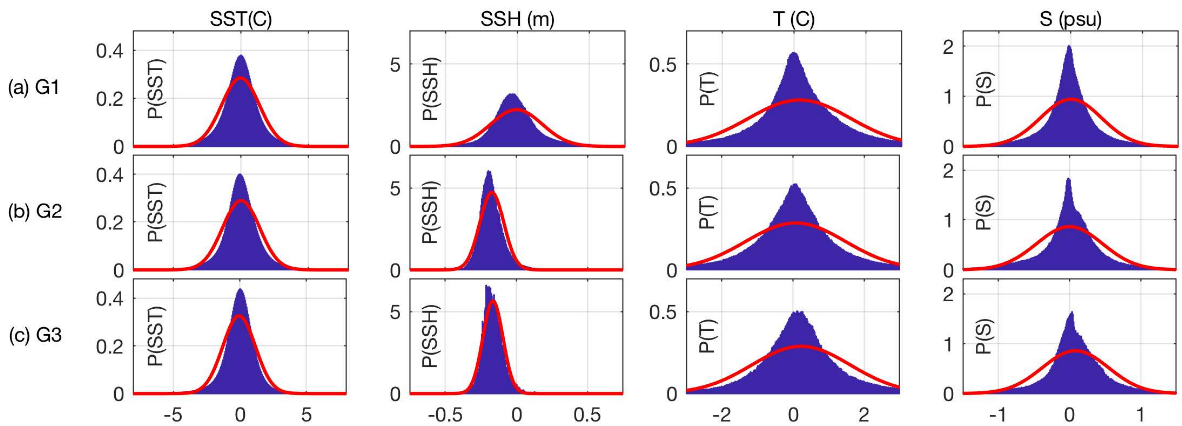

Figure 3: Probability density functions (pdfs) for the innovations in SST, SSH, *in situ T*, and *in situ S* based on *all* 4D-Var cycles for grid (a) G1, (b) G2, and (c) G3. A normal distribution with the same mean and standard deviation as the innovations is also shown for reference (red line).

The fit of the 4D-Var analyses to the observations is presented in Fig. 4, which shows time series of ratio of the final and initial values of $J_o = (\boldsymbol{H}\delta\boldsymbol{x} - \boldsymbol{d})^T \boldsymbol{R}^{-1} (\boldsymbol{H}\delta\boldsymbol{x} - \boldsymbol{d})$, the contribution of the observations to the incremental 4D-Var cost function, for all temperature observations (SST and *in situ*) and the observations of the zonal component of velocity, *u*. Figure 4 indicates that the largest reduction in J_o occurs during the 1st outer-loop. This is the case for all data types assimilated (not shown). In addition, Fig. 4 shows that while the fractional reduction in J_o associated with observations of temperature is similar in all three grids, the decrease in J_o for *u* increases with increasing resolution indicating that the model is able to capture the sub-mesoscale variability in ocean currents more effectively. This is discussed in detail in Part II.

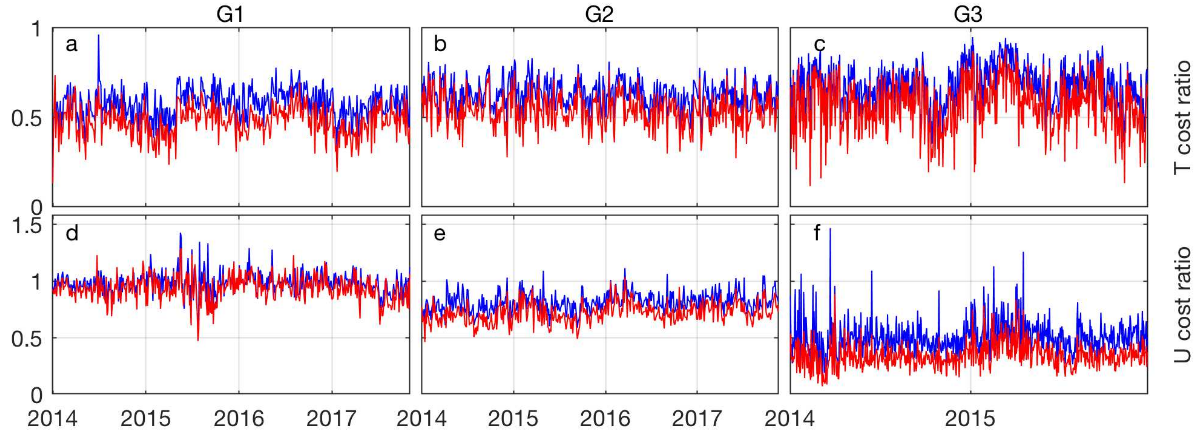

Figure 4: Time series of the ratio of the final and initial values of J_o for the 1^{st} outer-loop (blue line) and the 2^{nd} outer-loop (red line) of each 4D-Var cycle for all observations of temperature on grid (a) G1, (b) G2, and (c) G3, and for observations of zonal velocity on (d) G1, (e) G2, and (f) G3.

The surface forcing increments are generally small for both the G1 and G2 analyses and over most of the domain are just 1-2% of the seasonal standard deviation of the background fluxes.

4 Circulation Indexes

As noted in Section 1, a dominant feature of the circulation in the MAB is the front that separates the warm salty waters of the Gulf Stream from the cooler and fresher waters of the continental shelf. Significant excursions of the frontal location occur in association with numerous cross-shelf exchange processes. Processes known to contribute significantly to cross-shelf transport include frontal instabilities, meandering and eddy fluxes, wind forcing, saline intrusions within the pycnocline, vertical mixing, upwelling within the bottom boundary layer, and Gulf Stream ring interactions with the shelf (Gawarkiewicz *et al.*, 2018). An example of the latter is illustrated in Fig. 1, which shows the 4D-Var analyses of sea surface salinity (SSS) on 16 May 2014 on all three grids. A streamer of saline water associated with a large Gulf Stream ring can be seen impinging on the shelf. This particular event has been studied in detail by Zhang and Gawarkiewicz (2015) and is captured well in the ROMS 4D-Var analyses on all three grids. Figure 1 shows very clearly how the 4D-Var circulation estimates can capture sub-mesoscale secondary circulations as the grid resolution increases.

The observation impact indexes, I, considered here were chosen to target the position of the MAB front and quantify the magnitude of cross-shelf exchange fluxes, particularly concerning the OOI Pioneer Array.

4.1 Frontal Location

The MAB front has traditionally been associated with the position of the 34.5 isohaline, and the point where this isohaline intersects the bathymetry is often used as a proxy for the foot of the front (Beardsley *et al.*, 1985; Linder and Gawarkiewicz, 1998). Onshore excursions of the front foot are associated with upwelling favorable conditions (Castelao *et al.*, 2008) where offshore Ekman transport is balanced by onshore flow near the bottom (Lentz *et el.*, 2003), and such events are thought to be an important factor in the supply of nutrients to the continental shelf (Siedlecki *et al.*, 2011). Following the generally accepted aforementioned definition, a index was used that quantifies the change in the average front location based on the area between the position of the foot of the front in the background estimate $\boldsymbol{x}^b$ and the front foot position in the analysis $\boldsymbol{x}^a$. Specifically

$$I_f = \int_{\xi_1}^{\xi_2} \big(\eta(\xi) - \eta^r(\xi)\big) d\xi \tag{3}$$

where (ξ, η) represent the local Cartesian coordinates of the 4D-Var cycle-average position of the front foot, and $\eta^r(\xi)$ is a reference line. Thus, I_f represents the total area between the front foot location and the reference line. The integral in (3) was performed along the benthic isoline that defines the front foot as it crosses the Pioneer Array operations domain, which represents the endpoints ξ_1 and ξ_2. Since the front is a dynamic feature, ξ_1 and ξ_2 vary from one assimilation cycle to the next. The reference line chosen for $\eta^r(\xi)$ is the seasonally varying climatological position of the front foot, although the location of the reference line is unimportant since the index increment is given by:

$$\Delta I_f = \int_{\xi_1}^{\xi_2} \Big(\eta^a(\xi) - \eta^b(\xi)\Big) d\xi \tag{4}$$

where superscripts *a* and *b* refer to the analysis and background, respectively.

This index differs fundamentally from the general case considered in section 2 in that (4) is not an explicit function of the state-vector $\boldsymbol{x}$. It is, therefore, necessary to linearize $\eta^a(\xi)$ about the background frontal location $\eta^b(\xi)$ in order to apply the adjoint-based approach described in section 2. If $\boldsymbol{r}^b = \xi^b \boldsymbol{i} + \eta^b \boldsymbol{j}$ represents the position vector of the coordinate pairs that define the position of the isohaline foot in the background, then it is easy to show that to 1st-order, the difference between the position vector of the isohaline in the analysis and the background, $\Delta\boldsymbol{r}$, in the direction of the background salinity gradient ∇S^b is given by $\Delta\boldsymbol{r} = \Delta S \nabla S^b / |\nabla S^b|^2$, where $\Delta S = S^a(\boldsymbol{r}^b) - 34.5$ and $S^a(\boldsymbol{r}^b)$ is the salinity of the analysis evaluated at the position of the foot of the background 34.5 isohaline.[1] Thus, a 1st-order approximation of the position of the foot of the front in the analysis is $\boldsymbol{r}^a = \xi^a \boldsymbol{i} + \eta^a \boldsymbol{j} \approx \boldsymbol{r}^b + \Delta\boldsymbol{r}$. In this way, the area $\Delta I_f = I_f(\boldsymbol{r}^a) - I_f(\boldsymbol{r}^b)$ can be expressed as a function of $\Delta\boldsymbol{r} = \Delta S \nabla S^b / |\nabla S^b|^2$ which itself is a function of the background state-vector $\boldsymbol{x}^b$ as required by (2).

[1] We chose to identify the displacement vector $\Delta\boldsymbol{r}$ in the direction of the gradient ∇S^b such that $\Delta S = S^a(\boldsymbol{r}^b) - 34.5 = \Delta\boldsymbol{r} \cdot \nabla S^b$. Thus we require $\Delta\boldsymbol{r} = \alpha\boldsymbol{n}$ where $\boldsymbol{n} = |\nabla S^b|^{-1} \nabla S^b$ is the local unit vector parallel to the background gradient and α is a scalar. Therefore, $\Delta S = \Delta\boldsymbol{r} \cdot \nabla S^b = \alpha |\nabla S^b|^{-1} \nabla S^b \cdot \nabla S^b = \alpha |\nabla S^b|$ in which case $\alpha = \Delta S |\nabla S^b|^{-1}$. Thus $\Delta\boldsymbol{r} = \alpha\boldsymbol{n} = \Delta S |\nabla S^b|^{-2} \nabla S^b$.

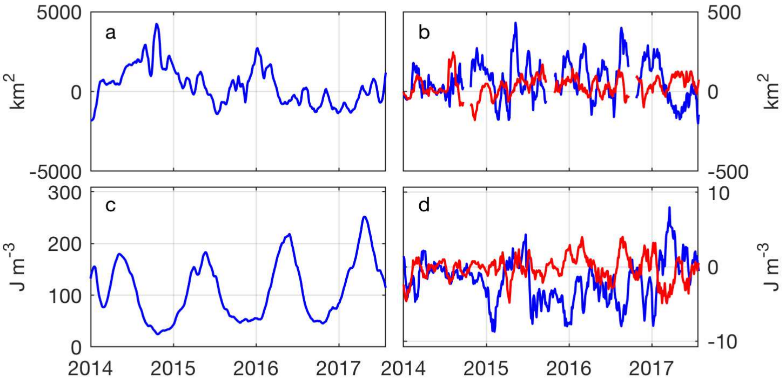

Figure 5: (a) Time series of the 30-day running mean I_f computed from the analysis $\boldsymbol{x}^b$ of each 4D-Var cycle on grid G1. Values of $I_f > 0$ ($I_f < 0$) indicate that the front has moved onshore (offshore) in the analysis compared to climatology. (b) Time series of the 30-day running mean increments ΔI_f representing the departures of the front location in the analysis $\boldsymbol{x}^a$ from the background position due to assimilating the observation during the 1st outer-loop (blue line) and 2nd outer-loop (red line) of each 4D-Var cycle on grid G1. Values of $\Delta I_f > 0$ ($\Delta I_f < 0$) indicate that the front has moved onshore (offshore) in the analysis compared to the background. (c) Time series of the 30-day running mean index I_e computed from $\boldsymbol{x}^b$ of each 4D-Var cycle on grid G1, and (d) time series of 30-day running mean ΔI_e, the increments that in I_e due to assimilating the observations. Similarly, the time series of ΔI_e in (d) are from the 1st outer-loop (blue line) and 2nd outer-loop (red line).

To illustrate, Fig 5a shows a time series of front foot index I_f computed from the background circulation $\boldsymbol{x}^b$ on grid G1. A 30-day running mean was applied to highlight more clearly the seasonal and interannual variations in I_f. Figure 5a indicates that the 4D-Var analysis tends to favor movements of the front foot onshore ($I_f > 0$). In contrast, offshore movements ($I_f < 0$) are typically smaller. Furthermore, while there is significant variability in I_f, there are no obvious interannual variations in the seasonal cycle. Time series of I_f on G2 and G3 are qualitatively and quantitatively similar to that shown in Fig. 5a for G1 (not shown). The mean and standard deviation of I_f on each grid is summarized in Table 3, indicating that the front foot statistics, as measured by this index, are similar across all three grids.

Index	**G1**	**G2**	**G3**
I_f (km^2)	263(1517)	216(1818)	240(1883)
I_e (J m^{-3})	112(57)	107(59)	98(47)
I_u (Sv)	-4×10^{-3}(2.1)	0.22(1.6)	0.41(2.0)
I_{uT} (kW m^{-2})	$-2\times10^{2}(4.5\times10^{2})$	$-1.9\times10^{2}(3.9\times10^{2})$	$-1.3\times10^{2}(3.6\times10^{2})$
I_{uS} (kg m^{-2} s^{-1})	$-9\times10^{-3}(2.7\times10^{-2})$	$-9\times10^{-3}(2.1\times10^{-2})$	$-5\times10^{-3}(1.7\times10^{-2})$

Table 3: The mean (standard deviation) of each index for the background circulation on each grid.

Time series of the foot front index increments ΔI_f that arise from assimilating the observations are shown in Fig. 5b for both the 1st and 2nd outer-loops. Again, there are no noticeable interannual variations in the seasonal cycle of the increment time series, which are characterized instead by irregular movements of the front onshore and offshore in response to 4D-Var corrections to the circulation. During the 1st outer-loop, the increments $\Delta I_f \sim 0.1 I_f$, while during the 2nd outer-loop, the ΔI_f are generally smaller. The mean and standard deviation of ΔI_f during both outer-loops, and for the 4D-Var analyses on all three grids, are presented in Table 4. On G1, the mean ΔI_f are positive indicative of a tendency for 4D-Var to correct for a mean offshore bias in the front foot location of the background. Table 4 shows that this bias is significantly reduced on G2 and changes sign on G3 but is close to zero.

4.2 Frontal Stratification

As a measure of the level of stratification associated with the front, we follow the work of Simpson and Bowers (1981), who studied fronts in the North Sea in terms of the potential energy required to thoroughly mix the upper part of water column. Specifically, we consider a index of stratification given by:

$$I_e = V^{-1} \iint g \int_D^{\zeta} (\bar{\rho} - \rho) z dz dA \qquad (5)$$

where ρ and $\bar{\rho}$ are respectively the *in situ* and vertically averaged density, both averaged over the assimilation window, D is a chosen depth, ζ is the free-surface displacement, and the area integral is performed over the Pioneer Array glider domain shown in Fig. 1c. The depth D was chosen to be the average depth of the front foot across the Pioneer Array glider domain. In (5), V represents the volume encompassed by the integrals with the result that I_e is the energy per unit volume (J m^{-3}) that is required to completely mix the upper D meters of the water column within the glider domain.

Figure 5c shows a time series of I_e computed from the 4D-Var analyses of G1. The seasonal cycle is associated with low values of I_e during the winter when the upper water column is fairly well mixed, and high values of I_e during the summer after the water column has re-stratified. Vertical sections of salinity during a typical minimum in I_e on 3 March 2016 and a typical maximum in I_e on 30 August 2016 are shown in Figs. 6a and 6b, respectively. During March, the MAB front is well defined within the Pioneer glider domain. The depth D over which the potential energy $I_e$in (5) is computed as the average depth of the front foot over the glider domain, and the intersection of the 34.5 isohaline with the bathymetry, which defines the front foot (*cf.* section 4.1), is clearly visible in Fig. 6a at a depth of around 75 m. Above this depth, the water column is well mixed over much of the glider domain, which accounts for the low value of I_e at this time of year. While the depth of the intersection of the 34.5 isohaline with the bathymetry is similar during August (Fig. 6b), the water column is strongly stratified over much of this depth within the glider domain, which accounts for the high value of I_e during this time. Thus, I_e can be a useful indicator of the "strength" of the front in terms of the mean stratification within the glider domain where low values of I_e correspond to situations where the front is well defined within the Pioneer target area, and vice versa for high values of I_e. Stratification is an important factor in this region since it also influences shelf-slope exchange via the development of instabilities (*e.g.*, Houghton *et al.*, 1988), onshore intrusions of saline waters from over the continental slope (Lentz, 2003), and the efficiency of vertical mixing.

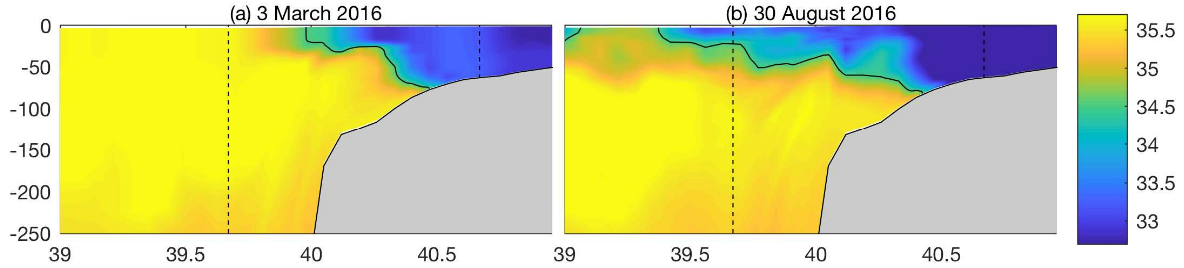

Figure 6: Vertical sections from G1 of salinity passing through the center of the Pioneer Array glider domain along 70.71°E on (a) 3 March 2016 and (b) 30 August 2016. The black contour is the 34.5 isohaline, and the intersection of this isohaline with the bathymetry defines the front foot. The black dashed lines mark the northern and southern edges of the glider sampling array shown in Fig. 1c.

Time series of I_e from G2 and G3 are both qualitatively and quantitatively similar to that shown in Fig. 5c (not shown). The mean and standard deviation of I_e on all three grids is shown in Table 3 and confirm that they vary within a similar range.

Time series of the increments ΔI_e arising from 4D-Var are shown in Fig. 5d for grid G1 for both outer-loops. During the 1st outer-loop, ΔI_e is generally negative for much of the time, indicating that 4D-Var is reducing the stratification and potentially strengthening the MAB front in the Pioneer target region. The increments during the 2nd outer-loop are typically smaller. However, during some periods, they partially offset those of the 1st outer-loop, indicating that, during some cycles, data assimilation reduces the stratification too much during the 1st outer-loop, and some re-stratification is necessary during the 2nd outer-loop so that the circulation is more consistent with observations. The mean and standard deviation of the increments ΔI_e are presented in Table 4 for all three grids. A negative bias is apparent on G1, suggesting that in this case, 4D-Var is largely correcting for bias in the stratification. Table 4 indicates that the bias is much reduced on G2 and is close to zero on G3, suggesting that in both cases, the stratification is more consistent with the observations.

4.3 Transport indexes

As noted earlier, there is also considerable variability in the cross-shelf exchange of water masses. Therefore, a series of indexes were also computed to quantify the impact of the observations on the 4D-Var estimates of conditions at the shelf-break in the vicinity of the OOI Pioneer Array. Specifically, we consider the following indexes:

$$I_u = \int_{s_1}^{s_2} \int_h^0 (\bar{u}_n - \tilde{u}_n) dzds \tag{6}$$

$$I_{uT} = \rho_o c_p A^{-1} \int_{s_1}^{s_2} \int_h^0 (\bar{u}_n - \tilde{u}_n)(\bar{T} - \tilde{T}) dzds \tag{7}$$

$$I_{uS} = 10^{-3} \rho_o A^{-1} \int_{s_1}^{s_2} \int_h^0 (\bar{u}_n - \tilde{u}_n)(\bar{S} - \tilde{S}) dzds \tag{8}$$

$$I_T = A^{-1} \int_{s_1}^{s_2} \int_h^0 (\bar{T} - \tilde{T}) dzds \tag{9}$$

$$I_S = A^{-1}\int_{s_1}^{s_2}\int_h^0(\bar{S}-\tilde{S})dzds. \qquad (10)$$

In each case, $\int_{s_1}^{s_s}\cdots ds$ represents an integral along a section of the h=200 m isobath, nominally identified as the location of the continental shelf-break. The vertical section chosen is indicated in each panel of Fig. 1 and cuts through the middle of the Pioneer Array. In (6) - (10), u_n corresponds to the component of the velocity that is locally normal to the section s, and an over-bar denotes the time average over each assimilation cycle. The tilde represents the mean seasonal cycle, and A is the area of the cross-section. Therefore, I_u, I_{uT}, and I_{uS} are measures of the departures from the mean seasonal cycle of the 4D-Var cycle average total volume transport, heat transport, and salt transport across the shelf. The indexes I_T and I_S are a measure of the departures from the mean seasonal cycle of the 4D-Var cycle average temperature and salinity along the section. They are used as additional diagnostics on G1 only.

Increment	G1			G2			G3		
	k=1	*k=2*	*r*	*k=1*	*k=2*	*r*	*k=1*	*k=2*	*r*
ΔI_f (km^2)	58(322)	30(182)	0.96	13(257)	17(130)	0.86	-6.6(60)	-3.5(35)	0.75
ΔI_e (J m^{-3})	-1.6(7.3)	-0.3(4.8)	0.99	-0.7(4.1)	-0.5(2.0)	0.96	-0.2(2.9)	-0.14(1.0)	0.77
ΔI_u (Sv)	-0.24(0.88)	-0.13(0.59)	0.97	-0.08(0.28)	-0.03(0.14)	0.98	-0.03(0.19)	-0.004(0.09)	0.97
ΔI_{uT} (kW m^{-2})	8.1(230)	-2.3(145)	0.90	9.6(115)	1.8(45)	0.96	7.9(51)	2.9(23)	0.96
ΔI_{uS} (kg m^{-2} s^{-1}) ×10^{-3}	2(13)	0.8(9)	0.91	0.3(5.9)	-0.05(2.7)	0.96	0.3(2.4)	0.04(1.3)	0.94

Table 4: The mean (standard deviation) of the increments in each index during the 1st outer-loop (*k=1*) and the 2nd outer-loop (*k=2*) on each grid. Also shown is the correlation coefficient *r* between the 1st outer-loop increment time series computed using the tangent linear assumption (2) and directly from the non-linear model solutions.

Figures 7a-e show time series of each index computed from the analysis state-vector $\boldsymbol{x}_a$. In the case of the transport indexes I_u, I_{uT}, and I_{uS} positive (negative) values represent onshore (offshore) transports relative to the mean seasonal cycle. Also shown in Figs. 7a-e are time series of the same indexes computed from a one-way nested run of the model without data assimilation subject to the same prior atmospheric conditions on all grids and the same Mercator-Océan open boundary conditions on G1. Figures 7a-c show that there is considerable variability on a range of time scales in the cross-shelf transports. Also, the transports are significantly modified by data assimilation. A closer inspection of the time series shows that periods of significant heat and salt transport are a combination of both the volume transport and changes in the mean temperature and salinity along the target section. Time series of I_u, I_{uT}, and I_{uS} for G2 and G3 (not shown) are comparable to those shown in Fig. 7 for G1. Table 3 summarizes the mean and standard deviations of the transport indexes on the three grids. For I_{uT} and I_{uS}, the mean and standard deviations are similar across all three grids, although, for I_u, there is an apparent onshore volume transport bias on G2 and G3.

The volume transport increments ΔI_u of Figs. 7f are generally small compared to I_u, indicating that data assimilation is not making large corrections to the circulation during each 4D-Var analysis. This is desirable behavior and suggests that the model is not subject to large adjustments and is mostly consistent with the new observations that are being assimilated. On the otherhand, the heat and salt transport index increments ΔI_{uT} and ΔI_{uS} of Figs. 7g and 7h are a more significant fraction of I_{uT} and I_{uS}, and are reflective of the changes in temperature and salinity increments across the target section (*cf.* Figs. 7i and 7j). In all cases, the increments during the 1st outer-loop are typically larger than during the 2nd outer-loop. It is also noteworthy that the increments in the transport index time series exhibit fluctuations on time scales similar to that of the model run without data assimilation, which suggests that 4D-Var is correcting changes in the circulation that are associated with the dynamic intrinsic variability on time scales longer than the 3-day assimilation windows.

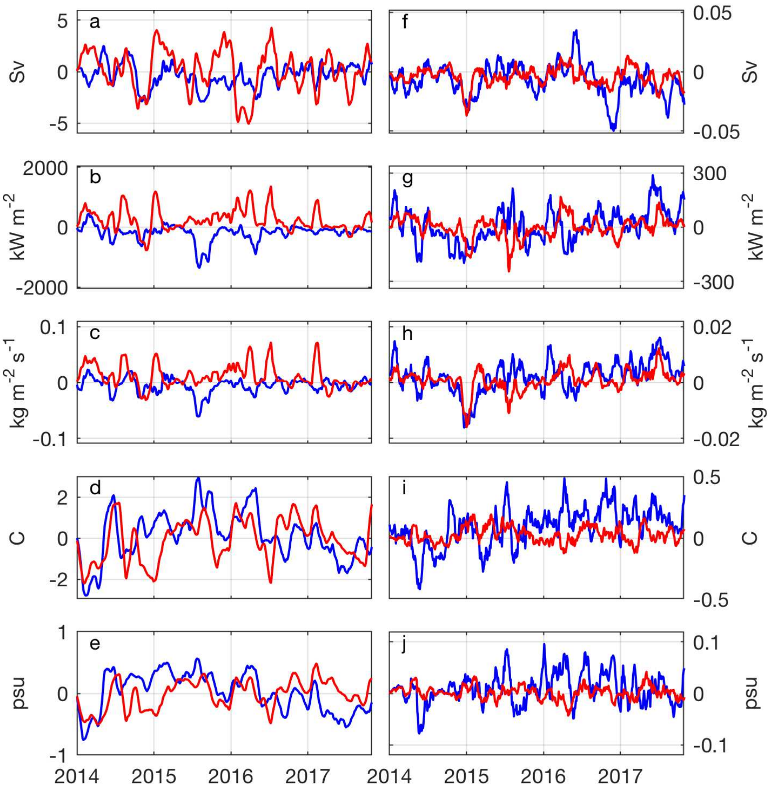

Figure 7: Time series of the 30-day running mean cross-shelf exchange indexes computed from the analysis circulation on grid G1 for each 4D-Var cycle (blue line) and the model run without data assimilation (red line): (a) I_u, (b) I_{uT}, (c) I_{uS}, (d) I_T, and (e) I_S. Time series of the 4D-Var increments are also shown for the 1st outer-loop (blue line) and 2nd outer-loop (red line): (f) ΔI_u, (g) ΔI_{uT}, (h) ΔI_{uS}, (i) ΔI_T, and (j) ΔI_S.

The mean and standard deviation of the increments in each index are summarized in Table 4 for both outer-loops on all three grids. On G1, the mean volume transport increments are offshore but close to zero on G2 and G3. Conversely, the mean heat and salt transport increments are onshore on all grids and decrease with increasing resolution.

5 Observation Impacts

Since two outer-loops are employed in the 4D-Var analyses, it is necessary to compute the observation impacts separately for each outer-loop. If $\boldsymbol{x}_n^a$ denotes the 4D-Var analysis at the end of the n^{th} outer-loop, then the observation impacts are quantified according to:

$$\Delta I_1 \approx \left(\boldsymbol{y}^o - H(\boldsymbol{x}^b)\right)^T \widetilde{\boldsymbol{K}}_1^T (\partial I/\partial \boldsymbol{x})|_{\boldsymbol{x}^b} \text{ and } \Delta I_2 \approx \left(\boldsymbol{y}^o - H(\boldsymbol{x}_1^a)\right)^T \widetilde{\boldsymbol{K}}_2^T (\partial I/\partial \boldsymbol{x})|_{\boldsymbol{x}_1^a}$$

where ΔI_1 and ΔI_2 represent the increment in the index I at the end of the 1st and 2nd outer-loop respectively, $\widetilde{\boldsymbol{K}}_1^T$ and $\widetilde{\boldsymbol{K}}_2^T$ are the reduced dimension Kalman gain matrices for each outer-loop, and $(\partial I/\partial \boldsymbol{x})|_{\boldsymbol{x}^b}$ and $(\partial I/\partial \boldsymbol{x})|_{\boldsymbol{x}_1^a}$ represent the derivatives of the index I evaluated using $\boldsymbol{x}^b$ and $\boldsymbol{x}_1^a$. Since $\boldsymbol{x}_1^a$ depends on the observation values, ΔI_2 cannot be unambiguously decomposed into the contributions from each observation. However, as discussed by Trémolet (2008), since $\Delta I_1 > \Delta I_2$, much of the impact of the observations on the final 4D-Var analysis can be attributed to the 1st outer-loop. This is also found to be the case here, as confirmed in Figs. 5 and 7, which show time series of ΔI_1 and ΔI_2 for each of the target indexes on G1. Similarly, the standard deviations in Table 4 confirm that the $\Delta I_1 > \Delta I_2$ on G2 and G3 also. Therefore, in the sequel, we will consider only the observation impacts during the 1st outer-loop.

It should also be noted that, with additional computational effort, ΔI_1 can be decomposed in the contributions from the different components of the control vector. However, preliminary analyses of ΔI_u (not shown) revealed that ~99% of the increment in volume transport is associated with the increment in the initial conditions. Therefore, in the sequel we have consider the total impact arising collectively from all elements of the control vector.

The impact of the observations on each index was quantified according to (2), which represents a 1st-order linearization of the index increment arising from data assimilation. Equation (2) shows that an important ingredient of these calculations is $(\partial I/\partial \boldsymbol{x})|_{\boldsymbol{x}^b}$. Since (4), (7), and (8) represent nonlinear indexes, computation of this first derivative is an additional linear approximation in the procedure. Therefore, before proceeding to compute the observation impacts, it is essential to test the veracity of the linear assumptions in (2). To this end, Table 4 shows the correlation coefficient r between the time series of the increments ΔI in each index computed from (2) and those calculated directly from the analysis and background estimates of I. In most cases, r exceeds 0.9, and in several instances is very close to 1. The lowest correlations are associated with I_f on G2 and G3 (0.86 and 0.75, respectively) and with I_e on G3 (0.77). Nonetheless, these correlations are still respectable and confirm that the linear approximations employed will yield reliable estimates of the observation impacts in these cases also.

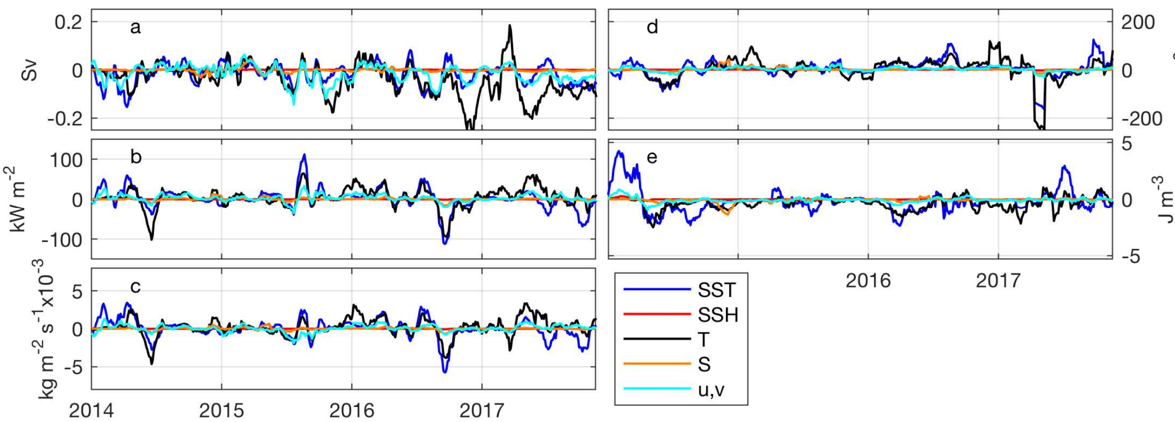

Figure 8: Time series from the G2 4D-Var analyses of the 30-day running mean of the contribution (aka *impact*) of each observation type to (a) ΔI_u, (b) ΔI_{uT}, (c) ΔI_{uS}, (d) ΔI_f, and (e) ΔI_e. Results are shown for the 1st outer-loop.

SST: satellite SST; *SSH*: satellite altimetry; *T, S*: *in situ* temperature and salinity observations; *u,v*: observations of velocity from HF radar and *in situ* moorings.

The contribution (aka *impact*) of each observing system to the increments ΔI of a chosen index will vary from cycle-to-cycle and depends on several factors including the number and distribution of the observations, the time evolution of the background circulation $\boldsymbol{x}^b(t)$, and the hypotheses about the background and observation errors described by $\boldsymbol{B}$ and $\boldsymbol{R}$. To illustrate, Fig. 8 shows time series from G2 of the impact of each type of observation on the 1st outer-loop increments in each of the indexes considered here. There are several noteworthy features of Fig. 8. Firstly, the relative impact of the various observing systems on a given ΔI changes through time, and it is not always the same type of observations that have the largest impact. Secondly, there is generally a great deal of consensus between the impact of observations from different platforms in that they usually have the same sign at any given time. However, there are a few periods where the impacts from different platforms are in opposition. Thirdly, the relative impact of each observation type during a particular time interval varies from index-to-index. In the G2 example shown, it is observations of temperature (remotely sensed and *in situ*) and velocity (HF radar and *in situ*) that exert the greatest control on all of the indexes. The impact of salinity observations is generally small on this grid, and the impacts of altimetry are generally negligible due to the limited size of the domain (*cf.* Fig. 1b) and the low number of satellite overpasses.

In the following sub-sections, the observation impact information encapsulated in time series such as Fig. 8 will be examined in different ways.

5.1 Impact vs. innovation

A useful diagnostic of the performance of the 4D-Var system is the impact of each observation compared to the corresponding innovation (*i.e.*, the difference between the observation and the background sampled at the observation point). To this end, Fig. 9 shows scatter plots of the impact of each observation on the foot front index I_f versus the innovation for each type of observation on all three grids. Each scatter plot can also be viewed as a contingency diagram and has the format of a 2-dimensional histogram showing the density of points that fall within each quadrant. The percentage of the total number of points that fall within each quadrant is also indicated.

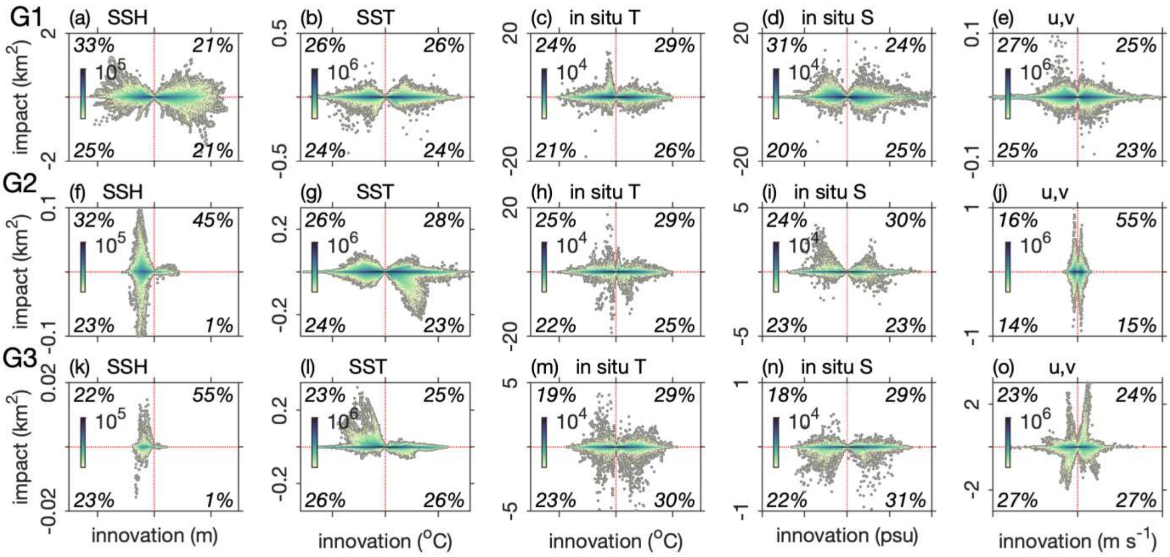

Figure 9: Scatter plots during the 1st outer-loop of impact vs. innovation for each observation type for (a-e) G1, (f-j) G2, and (k-o) G3 for the foot front index I_f. Also shown in color are 2D histograms of the number of points falling within selected bins. The red lines divide each panel into a contingency diagram, and the percentage of the total number of observations of the given type that fall within each quadrant is also shown. Note that for a given observation type, the scale on the ordinate varies from grid-to-grid (*i.e.*, down the columns).

Most of the scatter plots in Fig. 9 resemble "butterfly" wings in that observations associated with a small innovation (*i.e.*, instances where the model and observations are in excellent agreement) also have a little impact on I_f. As the innovation increases the range of impact that observations have on I_f becomes larger, as reflected by the "wing" structure. Furthermore, observations that are associated with very large innovations (*i.e.*, instances where the model and observations are in poor agreement) generally have a small impact on I_f. As noted in L19, this is a desirable feature of the 4D-Var system because very large innovations very likely represent cases of observations that have passed the quality control threshold through, say the coincidence of a poor background solution at a bad observation location, and we would not want these data to adversely impact the analysis. However, an inspection of the scatter plots also reveals some notable biases in the impacts, innovations, or both. For example, while the four quadrants of the scatter plot for SSH observations on G1 are fairly evenly populated (Fig. 9a), the corresponding scatter plots for G2 (Fig. 9f) and G3 (Fig. 9k) display a significant bias towards negative innovations, in agreement with Figs. 3b and 3c. Another interesting feature of Figs. 9g and 9l is that the scatter plots for SST observations on G2 and G3 exhibit a banded structure in one quadrant. In the case of G2 (Fig. 9g), many of the SST observations associated with positive innovations (*i.e.*, the model SST cooler than observed) have a pronounced negative impact on the I_f in that they tend to move the front further offshore. Conversely, on G3 (Fig. 9l), SST observations associated with negative innovations (*i.e.*, the model SST warmer than observed) impact the front foot location by moving it onshore. Further analysis reveals that these features are associated primarily with the AVHRR and AMSR, and further investigation is warranted.

Additional features of Fig. 9 that will be further discussed in the following sections include the general decline in the impact of the individual *in situ* temperature and salinity observations as grid resolution increases. In contrast, the impact of individual velocity measurements increases going from G1 to G3 (*cf.* Figs. 9e, 9j, and 9o).

Scatter plots associated with the other indexes share many qualitative features in common with those of Fig. 9 (not shown), although other detailed features related to bias in the innovations, bias in the impacts, or bias in both are specific to different indexes. Other scatter plot examples for the transport index on G1 are presented and discussed in L19.

5.2 RMS impacts

The observation impacts associated with each observation shown in the scatter plots of Fig. 9 can be parsed in various ways that highlight different aspects of the performance of the 4D-Var systems, and the role played by different observing platforms in affecting circulation changes.

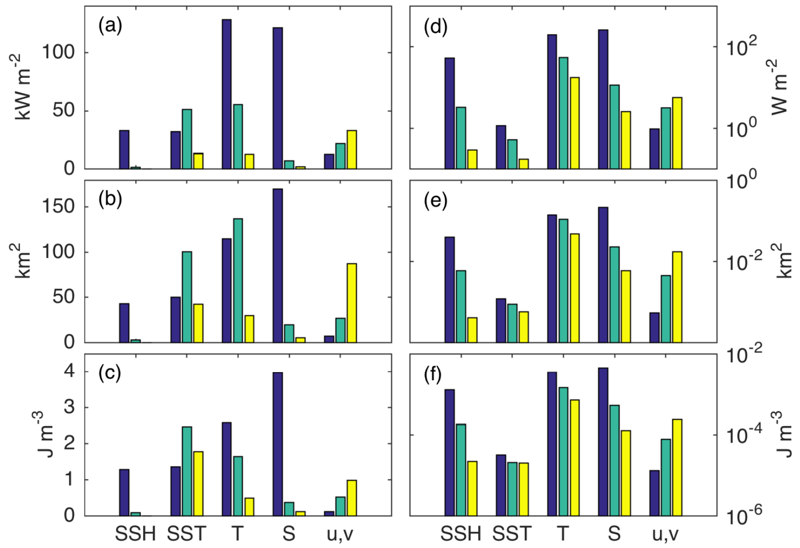

Figure 10: Histograms of the RMS impact averaged over all 4D-Var cycles of each observation type on (a) I_{uT}, (b) I_f, and (c) I_e for G1 (blue), G2 (green), and G3 (yellow). *SSH* – satellite altimetry; *SST* – satellite SST; *T, S* – *in situ* temperature and salinity; *u,v* – *in situ* or HF radar velocity measurements. Also shown are histograms of the RMS impact per datum of each observation type on (d) I_{uT}, (e) I_f, and (f) I_e for G1 (blue), G2 (green), and G3 (yellow). Note the log-scale in panels d-f.

Figures 10a-c show the root mean square (RMS) impact of each type of observation on I_{uT}, I_f, and I_e for all three grids. Figure 10a is representative of the other transport indexes I_u and I_{uS} also (not shown), as discussed in L19 for G1. Focusing first on remote sensing observations, for G1, the SST and SSH observations collectively have a similar impact even though there are two orders of magnitude fewer observations from altimetry (Fig. 2d). For G2, the collective impact of altimetry decreases with increasing grid resolution. This occurs for two reasons: first, as shown in L19, altimeter observations that are remote from the target section can have a significant impact on each index, which accounts for some of the high impact of SSH on G1. In addition, however, as Fig. 2 shows, the number of altimeter observations decreases considerably going from G1 to G3 because of the reduced geographical extent of each grid with increasing resolution. For SST, the impacts are higher on G2 than on G1, which is associated with a relatively large impact of these observations in the vicinity of the target section/region that defines each index (see also L19 in connection with G1). As Figs. 10a-c show, these local impacts carry over from G1 to G2 and G3.

Before discussing the impact of *in situ* observations, we reiterate that the observation impacts depend on several factors, including: (a) the background circulation $\boldsymbol{x}^b$, which, of course, is highly resolution-dependent across the three grids; (b) the background error covariance, $\boldsymbol{B}$; and (c) the observation error covariance, $\boldsymbol{R}$. The parameters used to compute $\boldsymbol{B}$ and $\boldsymbol{R}$ were not the same across all three grids since different error statistics are appropriate for each grid. Thus, some of the changes in the relative impact of various components of the observing system on the three grids will depend on unavoidable variations in the error covariances. It is important to remember that $\boldsymbol{R}$ is dominated by errors of representativeness which are difficult to estimate *a priori*. For *in situ* temperature observations, the standard deviations assumed for $\boldsymbol{R}$ are similar across all three grids and range from ~0.6°C on G1 to ~0.4°C on G2 and G3. However, *a posteriori* analysis of the innovation statistics, as described by Desroziers *et al.* (2005), suggests that these standard deviations should be closer to ~1°C. For *in situ* salinity observations, the *a priori* observation errors were assumed to ~0.2 on G1, while the *a posteriori* innovation statistics indicate that a more appropriate choice is ~0.4, which is the value used for both G2 and G3. Similarly, for velocity measurements, the standard deviation of the observation error on G1 was assumed to be ~0.6 ms^{-1} for HF radar surface current estimates and ~0.3 ms^{-1} for moorings. These values were adjusted downwards to ~0.1 ms^{-1} for HF radar observations and ~0.04 ms^{-1} for moorings for both G2 and G3 and are more in line with the *a posteriori* innovation statistics. While we would ideally like to compare cases where, say, only the model resolution is varying in the 4D-Var analyses across the three grids, the high computational expense of these calculations precludes running a more detailed and controlled suite of experiments, so we must draw on what we have. Nevertheless, variations in the level of errors across the different grids provide an indication of their control on the impacts.

Returning to Fig. 10, an obvious feature of Figs. 10a-c is that *in situ* observations have the largest impact on G1 for all three indexes, even though the number of *in situ* observations is an order magnitude less than the number of satellite SST observations (see Fig. 2d). *In situ* temperature observations maintain a relatively high impact on G2, although there is a significant decline on G3. This is partly because of the substantial reduction in the volume of observations and the loss of some remote impacts, but also because of the increasing influence of velocity observations on the sub-mesoscale circulation that is resolved by G3 (see Part II). Much of the dramatic decline in the impact of *in situ* salinity observations on G2 and G3, when compared to G1, is most likely associated with the difference in the assumed level of observation error. On G1, the level of observation error is probably too low, so the 4D-Var analyses are drawing more heavily on these data than on G2 and G3. However, there are other dynamical controls as well associated with geostrophic adjustment, as discussed in Part II.

On G1, velocity observations have a relatively small impact on all indexes, partly because of the high value assumed for the errors of representativeness, but also because of dynamical controls (see Part II). The impact of velocity observations increases from G1 to G2 and then again from G2 to G3 mainly because current measurements from the Pioneer Array moorings play an increasingly greater role in shaping the sub-mesoscale circulation as grid resolution increases. This is discussed in more detail in Part II.

While Figs. 10a-c represent the aggregate average impact of different observation types on the target indexes, Fig. 2 shows that there is considerable disparity in the number of observations of each type that are assimilated into the model. Therefore, it is informative to normalize the observation impacts by considering the RMS impact *per datum*, which is shown in Figs. 10d-f. Note that super-observations are considered as a single datum. Figures 10d-f show that *in situ* observations have by far the largest impact per datum for all indexes and across all grids. As discussed by L19, each SSH observation on G1 is ~50 times more impactful than an individual SST observation. This carries over to some extent to G2 as well, although the factor decreases to ~7 because the impact of SSH observations that are remote from the target sites is lost. On G3, the impact per datum of SSH and SST is similar because there are so few SSH observations to impact the circulation estimates.

Figures 10d-f show that, in general, except for the case of velocity observations, the observation impact per datum decreases with increasing resolution and decreasing domain size. This is most likely a combination of two factors: (i) as resolution increases the model can capture more faithfully the mesoscale and sub-mesoscale circulation features, and (ii) as shown in Table 2, the decorrelation length assumed for the background errors decreases with increasing resolution so the radius of influence of each observation will be correspondingly smaller moving from G1 to G3.

5.3 Observation impact as an indicator of 4D-Var performance

As discussed by Trémolet (2008), the impact of each observation on the analysis or ensuing forecast can be tracked line-by-line through the data assimilation code. This provides a powerful means for monitoring the performance of the 4D-Var system at various levels and different stages of the calculation. In ROMS, the observation impacts are evaluated during each inner-loop iteration, and provide a quantitative measure of how the observations are being utilized during the assimilation procedure. To illustrate, Fig. 11 shows the RMS impact of each observation type on I_u and I_e on all grids during each inner-loop of the two outer-loops employed.

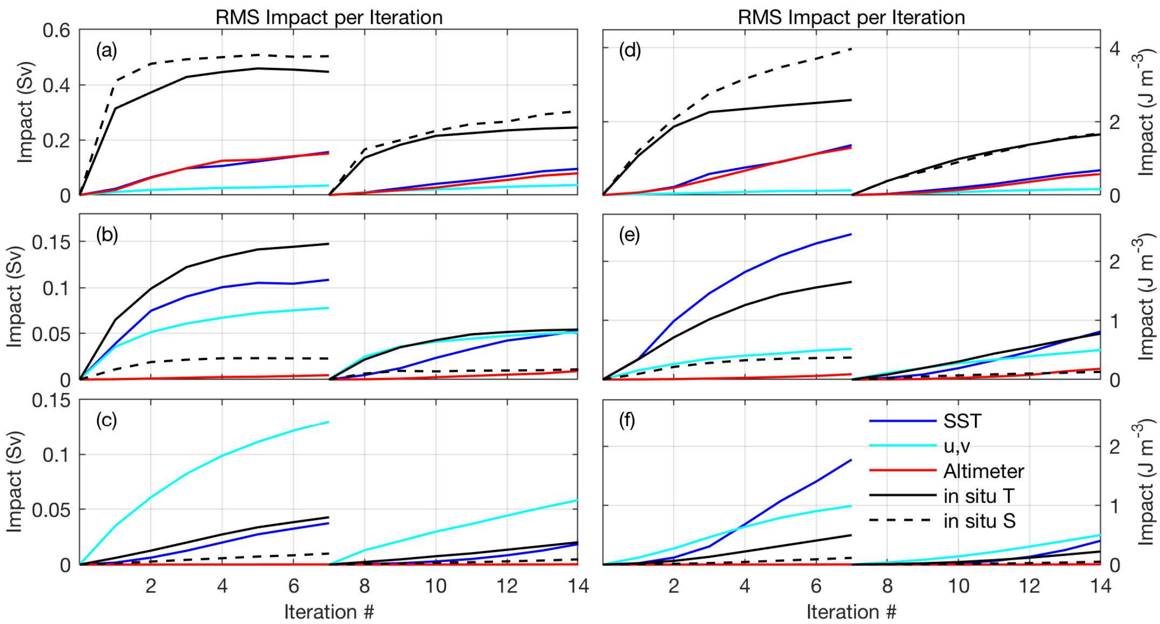

Figure 11: The RMS impact of each observation type versus 4D-Var iteration number for ΔI_u averaged over *all* 4D-Var cycles for (a) G1, (b) G2, and (c) G3. Each 4D-Var cycle comprises two outer-loops and seven inner-loops, for a total of 14 iterations in all. At the end of the 1st outer-loop, the background circulation is updated at which time the impact is reset to zero. SST – satellite SST; u,v – *in situ* and HF radar current observations; Altimeter – along-track altimetry; *in situ* T, S – *in situ* temperature and salinity observations. The RMS impacts per iteration for ΔI_e are also shown for (d) G1, (e) G2, and (f) G3.

On G1, Figs. 11a and 11d confirm the dominant role played by *in situ* observations of T and S in controlling I_u and I_e. For these data, Figs. 11a reveals that for I_u, during the 1st outer-loop, the impacts asymptote to a near-constant value after just three inner-loops. For I_e (Fig. 11d), the impacts of *in situ T* exhibits similar behavior. However, for *in situ S*, the impacts continue to trend upwards even after seven inner-loops indicating that there is more useful information to be utilized from these data. The aggregate impact of SST and SSH on G1 is similar for both indexes (Figs. 11a and 11d), consistent with Figs. 10a-c, and also show a continuing upward trend at the end of the 1st outer-loop, indicating that there is additional useful information that could be extracted from these data too. Figure 11 also confirms that the observation impacts during the 1st outer-loop are larger than those during the 2nd outer-loop. The indexes I_{uT}, I_{uS}, and I_f exhibit similar characteristics (not shown but see also L19).

On G2, satellite SST and velocity observations emerge to play a more dominant role, as shown in Figs. 11b and 11e. In this case, altimetry plays a minor role and the impact *in situ S* has been largely relegated, as noted in section 5.2. In the case of I_e, SST observations have the most impact. For both I_u and I_e on G2, the impact of the dominant data types continues to exhibit an upward trend at the end of the 1st outer-loop suggesting that the 4D-Var analyses on this grid may benefit from additional inner-loops. The indexes I_{uT}, I_{uS}, and I_f exhibit similar characteristics (not shown).

On G3, velocity observations emerge as generally the most impactful observations for I_u (Fig. 11c). The impact of these data is also significant for I_e (Fig. 11f), but velocity loses its poll position to SST observations after four inner-loops. For both I_u and I_e, the continued upward march of the observation impacts at the end of the 1st outer-loop indicates that additional inner-loops could be beneficial on G3 also. Similarly, for the indexes I_{uT}, I_{uS}, and I_f (not shown).

6 Remote Sensing Observation Impacts

The geographical distributions of the observation impacts associated with satellite observations are particularly revealing, and display what we believe are the signature of the dynamical processes that are responsible for conveying information from the observations to the target sites that define the impact indexes *I*. With this in mind, Fig. 12 shows the RMS *impact per datum* of all SST observations that fall within each model grid cell. The cases shown are for I_{uT}, I_f, and I_e on all three grids.

For G1, Figs. 12a-c reveal the presence of large-scale, coherent patterns of impact for SST that are common to all three indexes. These same patterns are present for I_u and I_{uS} also (not shown), and, as discussed in L19, are associated with the underlying dynamics of the circulation and the structure of the inverse total error covariance matrix in observation space $(\boldsymbol{HBH}^T + \boldsymbol{R})^{-1}$ (aka the inverse stabilized representer matrix) which lies at the heart of the analysis equation (1). In particular, Figs. 12a-c show regions of elevated impact that are both local to the index target regions and remote, such as the north wall of the Gulf Stream.

Figures 12d-f show that the geographical distributions of SST impacts on G2 for the three indexes shown also share common features. The most apparent features are the high impacts extending upstream from the target areas that are associated with the equatorward flowing shelf-break jet, and the tongue of high impact associated with flow exiting the Gulf of Maine through the Great South Channel that defines the western edge of Georges Bank. Similar features are present on G1 also (Figs. 12a-c). As in G1, it is likely that these features common to all of the indexes, including I_u and I_{uS} (not shown), are controlled by the combined influences of the background circulation $\boldsymbol{x}_b$ and *prior* assumptions assumed in the 4D-Var procedure via the inverse stabilized representer matrix $(\boldsymbol{HBH}^T + \boldsymbol{R})^{-1}$.

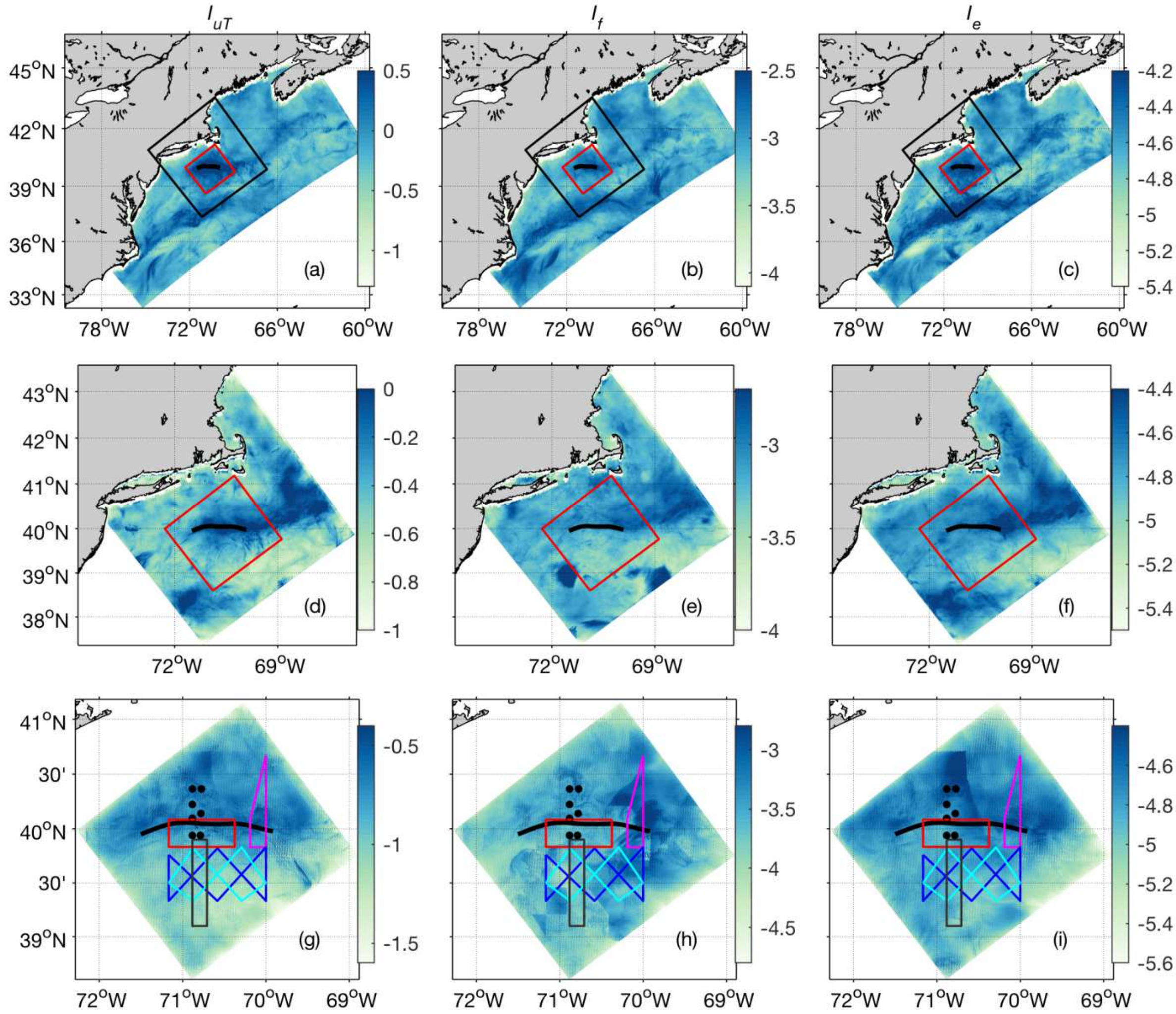

Figure 12: Log$_{10}$ of RMS impact per datum for satellite SST observations that fall within each model grid cell for indexes I_{uT}, I_f, and I_e on (a-c) G1, (d-f) G2 and (g-i) G3. The target section used for the transport indexes is indicated in each panel by the bold black line. The location of the G2 and G3 grids are indicated by the rectangles in a-c as is the G3 grid in d-f. The location of the Pioneer moorings (black dots) and the nominal Pioneer glider sampling array is shown in g-i. Recall that the Pioneer glider array is the target region used to define I_f and I_e.

In the case of G3, Figs. 12g-i show that while there is some commonality in the geographic distribution of the SST impacts, most conspicuously associated with the shelf-break jet, there are also some significant differences. The differences are probably a reflection of the more complex nature of the flow of information through the G3 4D-Var analyses due to the intricacies of the sub-mesoscale environment (*cf.* Fig. 1c). This is a topic that warrants further exploration, but as shown by L19, the analysis of the factors controlling the characteristic patterns of impact is rather involved. The "patchwork" patterns apparent in Figs. 12g-i are associated with variations in SST coverage of the different observing platforms. For example, WSAT is a microwave instrument with a low resolution foot print that covers only part of the G3 domain.

The geographical distributions of the RMS impacts of altimetry observations also display interesting and dynamically controlled patterns of local and remote influence, as shown in detail by L19 for G1. Similarly, while not shown here, SSH impacts on the G2 circulation indexes share some similarities with their G1 counterparts. In the case of G3, the altimeter coverage during the 2014-15 period considered is fairly sparse, so it not so easy to identify robust geographical distributions of impact in this case.

As discussed in L19, some aspects of the local and remote impacts apparent in Fig. 12 can be understood in terms of "information horizons" (see also Moore *et al.*, 2015) - the distance over which information contained in the observations can travel via the processes of wave propagation and advection. L19 estimate that during a typical 3-day assimilation cycle, as employed in G1 and G2, the information horizon associated with horizontal advection is ~25 km for the shelf-break jet and ~500 km for the Gulf Stream. The information horizon associated with internal waves is estimated to ~500 km also, while information carried by barotropic waves can reach every point in the model domain.

7 In Situ Observation Impacts

The impact of *in situ* observations on the 4D-Var analyses on G1, G2, and G3 is the subject of Part II, with a particular focus on the NSF OOI Pioneer Array. In this section, we present a broad overview of the *in situ* observation impacts, and the interested reader is encouraged to consult Part II for a more detailed account.

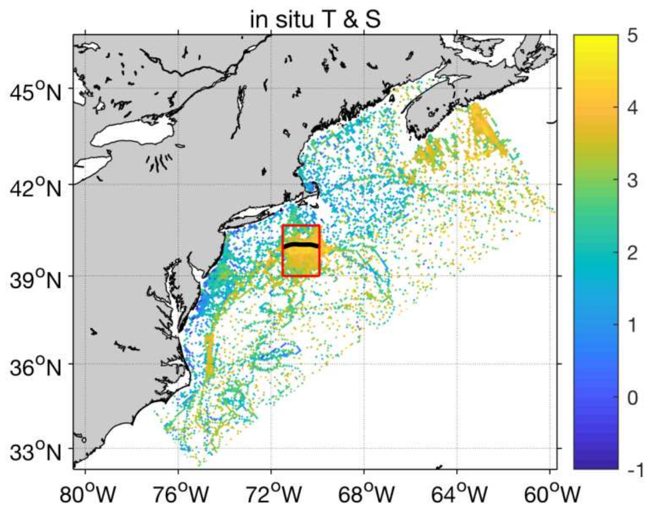

Figure 13: Log_{10} of the vertically integrated RMS impact per datum for *in situ* temperature and salinity observations combined that fall within each horizontal model grid cell for I_{uT} on G1 for the 1st outer-loop. The bold black line indicates the target section used for the transport index. Also shown is the nominal extent of the Pioneer glider array (red box).

Figure 10 shows that *in situ* observations of temperature and salinity have the largest impact on all indexes on G1, both on aggregate (Figs. 10a-c) and in terms of the *impact per datum* (Figs. 10d-f). The geographic distribution of the vertically *integrated* RMS observation impact for *in situ T* and *S* combined is illustrated in Fig. 13 for the cross-shelf heat transport index I_{uT}. As in the case of SST (Fig. 12a), the *in situ* observations exhibit impacts that are both local and remote from the target section. In this case, the influence of observations downstream along the shelf-break current is a marked feature, as is the upstream impact of the dense set of observations by gliders and hydrographic surveys on the Scotian Shelf. While observations on the Scotian Shelf help constrain the modeled equatorward inflow from the north that is subsequently partitioned between entering the Gulf of Maine or following the shelf-break south of Georges Bank toward the Pioneer Array site (Lopez *et al.* 2020), the time scale of this transport far exceeds the 3-day analysis interval of the observation impacts. This distant teleconnection is, however, well within scope for the influence of freely propagating coastal trapped waves (CTW). Brunner *et al.* (2019) calculate that the mode 1 free CTW at the Pioneer site has a phase speed of some 7 m s^{-1}. At this speed, CTWs originating on the Scotia Shelf in response to the data assimilation adjustments will traverse the 900 km to the Pioneer Array, via the continental slope wave guide, within 1.5 days. As in the case of SST and SSH, the geographic distribution of the *in situ* hydrographic observations is relatively robust across *all* metrics considered here (not shown).

Figure 10 also shows that while the aggregate impact of *in situ* hydrographic observations generally declines going from G1 to G3, the impact per datum of these data remains relatively high. The geographic distribution of the observation impacts exhibits robust features on G2 and G3 across all indexes (not shown) and will be discussed in more detail in Part II.

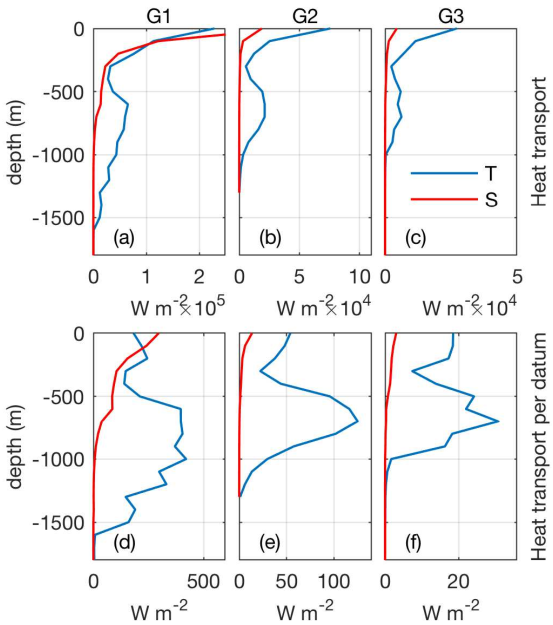

Figure 14: RMS impact versus depth of all *in situ* temperature (blue line) and salinity (red line) observations on ΔI_{uT} averaged over all 4D-Var cycles during the 1st outer-loop for (a) G1, (b) G2, and (c) G3. The RMS impact per datum versus depth for the same index is shown for (d) G1, (e) G2, and (f) G3.

The aggregate RMS impact on I_{uT} of *in situ* observations of T and S versus depth is illustrated in Figs. 14a-c for all three grids. For G1 (Fig. 14a), the impact of T and S is similar in the upper 400 m of the water column, although, below this depth, the temperature observations dominate. For G2 and G3, the impact of S is diminished compared to G1, consistent with Figs. 10 and 11. The vertical profiles of temperature impacts are similar across all three grids, and in each case indicate the presence of elevated impact in the range ~500-1000 m. The RMS *impact per datum* versus depth for T and S is shown Figs. 14d-f, which highlights the influence of subsurface temperature observations in the 500-1000 m depth range. Profiles of observation impacts for T and S for the other indexes display qualitatively similar features to those shown in Fig. 14 (not shown).

The RMS impacts of velocity observations versus depth are shown in Fig. 15 again for I_{uT}, although the main features are qualitatively similar for the other indexes (not shown). The aggregate impacts of Figs. 15a-c indicate that velocity observations in the upper 100 m of the water column have the largest impact. The impact also increases going from G1 to G3, in keeping with Figs. 10 and 11. The RMS *impact per datum*, on the other hand, is relatively uniform below about 20 m (Figs. 15d-f). While most of the surface velocity observations are from HF radar estimates, the majority of subsurface measurements are from the Pioneer Array moorings, which measure currents down to ~75 m on the shelf and ~400 m beyond the shelf-break.

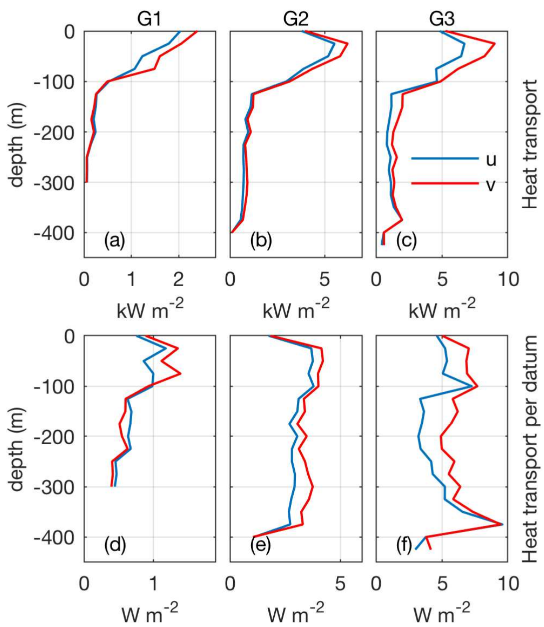

Figure 15: RMS impact versus depth of all *in situ* zonal (blue line) and meridional (red line) velocity observations on ΔI_{uT} averaged over all 4D-Var cycles for (a) G1, (b) G2, and (c) G3. The RMS impact per datum versus depth for the same index is shown for (d) G1, (e) G2, and (f) G3.

8 Summary and Conclusions

A state-of-the-art 4-dimensional variational data assimilation system has been applied in a three-level nested configuration of ROMS to compute estimates of the time-evolving ocean circulation in the Mid-Atlantic Bight, with a particular focus on the region served by the NSF OOI Pioneer Array. The outer-most model grid forms the basis of the near real-time analysis forecast system that is currently run in support of the U.S. IOOS MARACOOS regional association (Levin et al., 2018; Wilkin *et al.*, 2018) in which observations of the ocean from a broad range of remote sensing and *in situ* platforms are assimilated. In the nested configuration considered here, a wide range of circulation regimes are well represented, spanning the western current, the energetic mesoscale eddy field, and the complex sub-mesoscale circulation that is populated by ephemeral frontal features. While these are all challenging circulation environments for any data assimilation system, various diagnostic system indicators demonstrate that 4D-Var performs well across all three domains.

The primary goal of this study is to quantify the direct impact that observations from the various observing platforms that serve the MARACOOS region have on different aspects of the ocean circulation. Here the specific focus has been on the MAB shelf-break front, and associated slope-shelf exchange processes in the vicinity of the Pioneer Array since a goal of this component of the OOI is to explore the dynamics that control these processes. With this in mind, several indexes of the circulation were considered as quantitative indicators of different aspects of the dynamics in the vicinity of the shelf-break front. Specifically, we considered the location of the front, the strength of the associated stratification, and the cross-shelf transport of mass, heat, and salt. As one might expect, significant differences exist between 4D-Var solutions and a one-way nested free-running model. Also, 4D-Var leads to significant increments in the chosen circulation indexes on time scales that are similar to the intrinsic variability of the free model, indicating that 4D-Var is not just merely making reactionary corrections to the ocean state in response to the model-minus-observation differences, but is also informing the evolution of the circulation on a range of time scales in a dynamically consistent way.

In this study, an adjoint approach, similar to that used operationally in numerical weather prediction, was used to quantify the impact of the observations on the 4D-Var increments in each chosen circulation index. The observation impacts were found to vary considerably in space and time depending on the number, type, and spatial distribution of the observations, the background circulation, and the statistics assumed *a priori* for the errors in the background and observations. However, the geographic distribution of the observation impacts was found to be robust across all of the indexes considered and across the three domains. Unravelling the dynamics of the pathways by which a particular observation influences the ocean state in the near- and far-field is a complicated and involved process. Clearly, there many "moving parts" in (2) used to compute the observation impacts. L19 explored broadly the contributions and influence of model dynamics via $\boldsymbol{H}$ and $\boldsymbol{H}^T$, and the error covariances $\boldsymbol{B}$ and $\boldsymbol{R}$ on the geographical distributions of the impacts. While many features of Fig. 12 can be understood conceptually in terms of the *information horizons* associated with the fundamental processes of horizontal advection and wave propagation, more detailed analysis needed to identify role of individual mechanisms.

It is useful to take a step back and remember what information the observation impact given by (2) provide. Equation (2) quantifies ΔI given the observations available $\boldsymbol{y}^o$, the *prior* hypothesis about errors in the observations (via $\boldsymbol{R}$), errors in the background (via $\boldsymbol{B}$), and hypotheses about the dynamics that control the ocean state (via $\boldsymbol{H}$). Furthermore, the contribution of each observation to the dot-product that defines ΔI is unambiguous and is a reflection of all the assumptions and hypotheses that we have made. The observation impact calculation will not, however, directly confirm or nullify these assumptions of hypotheses because if we change any aspect of the data assimilation system or the model, then the circulation estimates will change, and so too will the observations impacts. However, some aspects of the relative impacts of different observation types will obviously be robust since these are controlled by the dynamics and physics of the ocean. Nevertheless, observation impact calculations like those presented here provide a quantitative measure of the relative *value* of observations from different observing platforms. Such information is of considerable value to decision makers since one could make a case for maintaining certain observing platforms based on the important (or critical) role they play in controlling some aspect of the state estimates. And, of course, one could use the quantitative information that observation impact calculations provide to argue for increasing the coverage or level of redundancy of particularly impactful platforms.

Our results shows that there is generally a reasonable degree of consensus between the impacts of different observation types and observing platforms, indicating that the 4D-Var system can make efficient use of complementary information from multiple sources. On the other hand, there is also considerable temporal variability in the relative impact of different observation types. And, as noted, the impact of a particular kind of observation varies across the three domains as a result of changes in data density, assumptions about error statistics, and the change in the dynamical circulation regime (see Part II for more analysis of the latter point).

The observation impacts are also a valuable tool for monitoring the efficacy of data streams and different components of an observing system. For example, significant changes in the impact of a particular data stream over time may be an indication of problems that are developing with the instrument or the data stream itself. Scatter diagrams like those in Fig. 9 can be used to identify outliers, and, anecdotally, there have been instances in our own work where improvements were made to the quality control of some remotely sensed data that were identified as problematic in this way. Furthermore, observation impact monitoring provides information about the performance of the 4D-Var system, as in Fig. 11. Clearly, there are some observation types for which there is a continuing upward trend in the observation impact at the time that the 4D-Var calculations are terminated, indicating that there is more useful information that can be mined from such data by further tuning of the 4D-Var system.

Other calculations closely related to those presented here quantify the *sensitivity* of ocean state estimates to changes in the observation values, or indeed the observing system. By combining observation *impact* and observation *sensitivity* information, the degree of synergy between different observing platforms can be quantified. This idea was introduced in L19 and is developed further in Part II (Levin *et al.*, 2020) in which we explore in detail the role played by the Pioneer Array observing system in shaping the MAB circulation estimates.

Finally, we note again that the observation impact methodology employed here can also be applied to the forecast problem. In this case, the extent to which each observation improves or degrades forecast skill, as measured by a metric I, can be quantified. This type of analysis has been a mainstay in operational numerical weather prediction for some time and is now an important emerging activity in some near real-time ocean analysis systems as well. ROMS is at the forefront of these activities and is being used in this capacity, and the results of ongoing forecast observation impact studies will be the subject of future publication.

Acknowledgements

This work was supported by grants from the National Science Foundation (OCE-1459665 and OCE-1459646), NASA (NNX17AH58G) and NOAA (NA16NOS0120020). Pioneer Array data were obtained from the NSF Ocean Observatories Initiative Data Portal http://ooinet.oceanobservatories.org.

References

Andersson, E., Järvinen, H., 1999. Variational quality control. *Q. J. R. Meteorol. Soc*. **125**, 679-722.

Balmaseda, M.A., Anderson, D.L.T., Vidard, A., 2007. Impact of Argo on analyses of the global ocean. *Geophys. Res. Letts*. **34**, L16605. http://dx.doi.org/10.1029/2007GL0304452.

Beardsley, R.C., Chapman, D.C., Brink, K.H., Ramp, S.R., Schlitz, R., 1985. The Nantucket Shoals Experiment (NSFE79), I, A basic description of the current and temperature variability. *J. Phys. Oceanogr.*, **15**, 713-748.

Boyer, T., Antonov, J., Baranova, O., Garcia, H., Johnson, D., Locarnini, R., Mishonov, A., OBrien, T., Seidov, D., Smolyar, I., Zweng, M., 2009. World ocean database 2009. In: Levitus, S. (Ed.), NOAA Atlas NESDIS 66, 216pp.

Brunner, K., Rivas, D., Lwiza, K. M., 2019. Application of Classical Coastal Trapped Wave Theory to High-Scattering Regions. *J. Phys. Oceanogr.*, **49**, 2201-2216.

Castelao, R., Glenn, S., Schofield, O., Chant, R., Wilkin, J., J. Kohut, J., 2008. Seasonal evolution of hydrographic fields in the central Middle Atlantic Bight from glider observations, *Geophys. Res. Lett*. **35**, L03617, doi:10.1029/2007GL032335.

Courtier, P., Thépaut, J.N., Hollingsworth, A., 1994. A strategy for operational implemenation of 4D-Var using an incremental approach. *Quart. J. R. Meteorol. Soc*. **120**, 1367-1388.

Desroziers, G., Berre, L., Chapnik, B., Poli, P., 2005. Diagnosis of observation, background and analysis-error statistics in observation space. *Q. J. R. Meteorol. Soc*. **131**, 3385-3396.

Drévillon, M., Bourdallé-Badie, R., Derval, C., Lellouche, J.M., Rémy, E., Tranchant, B., Benkiran, M., Greiner, E., Guinehut, S., Verbrugge, N., Garric, G., Testut, C.E., Laborie, M., Nouel, L., Bahurel, P., Bricaud, C., Crosnier, L., Dombrowsky, E., Durand, E., Ferry, N., Hernandez, F., Galloudec, O.L., Messal, F., Parent, L., 2008. The GODAE/Mercator-Ocean global ocean forecasting system: results, applications and prospects. *J. Oper. Oceanogr.* **1**, 51–57.

Fairall, C., Bradley, E., Hare, J., Grachev, A., Ebson, J., Young, G., 2003. Bulk parameterization of airsea fluxes: updates and verification for the COARE algorithm. *J. Climate* **16**, 571–591.

Fleming, N., 2016. Seasonal and spatial variability in temperature, salinity and circulation of the Middle Atlantic Bight. PhD thesis, 336pp.

Fratantoni, P., and R. Pickart, 2003. Variability of the shelf break jet in the Middle Atlantic Bight: Internally or externally forced. *J. Geophys. Res*, 108, 3166.

Fennel, K., J. Wilkin, J. Levin, J. Moisan, J. O'Reilly, D. Haidvogel, 2006. Nitrogen cycling in the Middle Atlantic Bight: Results from a three-dimensional model and implications for the North Atlantic nitrogen budget. *Global Biogeochemical Cycles*, **20**, GB3007, doi: 10.1029/2005GB002456.

Fujii, Y., Rémy, E., Zuo, H., Oke, P., Haliwell, G., Gasparin, F., Benkiran, M., Loose, N., Cummings, J., Xie, J., Xue, Y., Masuda, S., Simith, G.C., Balmaseda, M., Germineaud, C., Lea, D.J., Larnicol, G., Bertino, L., Bonaduce, A., Brasseur, P., Donlon, C., Heimbach, P., Kim, Y., Kourafalou, V., Le Traon, P., Martin, M., Paturi, S., Tranchant, B., Usui, N., 2019. Observing System Evaluation Based on Ocean Data Assimilation and Prediction Systems: On-Going Challenges and a Future Vision for Designing and Supporting Ocean Observational Networks. *Frontiers in Marine Science*, https://doi.org/10.3389/fmars.2019.00417.

Gawarkiewicz, G., Todd, R., Zhang, W., Partida, J., Gangopadhyay, A., Monim, M.U.H., Fratantoni, P., Malik, A.M., Dent, M., 2018. The changing nature of shelf-break exchange revealed by the OOI Pioneer Array. *Oceanography* **31**, 60–90.

Gratton, S., Tshimanga, J., 2009. An observation-space formulation of variational assimilation using a restricted preconditioned conjugate gradient algorithm. *Quart. J. R. Meteorol. Soc*. **135**, 1573–1585.

Gürol, S., Weaver, A., Moore, A., Piacentini, A., Arango, H., Gratton, S., 2014. B-preconditioned minimization algorithms for variational data assimilation with the dual formulation. *Quart. J. R. Meteorol. Soc.* **140**, 539–556.

Houghton, R., Aikman, F., Ou, H., 1988. Shelf-slope frontal structure and cross-shelf exchange at the New England shelf-break. *Cont. Shelf Res*. **8**, 687-710.

Langland, R., Baker, N., 2004. Estimation of observation impact using the NRL atmospheric variational data assimilation adjoint system. *Tellus* **56A**, 109–201.

Le Hénaff, M., De Mey, P., Marsaleix, P., 2009. Assessment of observational networks with the representer matrix spectra method-application to a 3D coastal model of the Bay of Biscay. *Ocean Dyn*. **59**, 3–20.

Lentz, S.J., Shearman, K., Anderson, S., Plueddemann, A., Edson, J., 2003. Evolution of stratification over the New England shelf during the Coastal Mixing and Optics study, August 1996–June 1997, *J. Geophys. Res*. **108**, 3008, doi:10.1029/2001JC001121.

Lentz, S. J., 2003. A climatology of salty intrusions over the continental shelf from Georges Bank to Cape Hatteras, *J. Geophys. Res*. **108**, 3326, doi:10.1029/2003JC001859.

Levin, J., Wilkin, J., Fleming, N., Zavala-Garay, J., 2018. Mean circulation of the mid-atlantic bight from a climatological data assimilative model. *Ocean Model*. **128**, 1–14.

Levin, J., Arango, H.G., Laughlin, B., Wilkin, J., Moore, A.M., 2019. The impact of remote sensing observations on cross-shelf transport estimates from 4D-Var analyses of the Mid-Atlantic Bight. *Advances in Space Research*, https://doi.org/10.1016/j.asr.2019.09.012

Levin, J., Arango, H.G., Laughlin, B., Wilkin, J., Moore, A.M., 2020. Observation Impacts on the Mid-Atlantic Bight Front and Cross-Shelf Transport in 4D-Var Ocean State Estimates: Part II – The Pioneer Array. *Ocean Modelling*, submitted.

Linder, C., Gawarkiewicz, G., 1998. A climatology of the shelf break front in the Middle Atlantic Bight. *J. Geophys. Res.* **102**, 18405–18423.

Lopez, A. G., Wilkin, J.L., Levin, J.C., 2020. Doppio – a ROMS (v3.6)-based circulation model for the Mid-Atlantic Bight and Gulf of Maine: configuration and comparison to integrated coastal observing network observations, Geosci. Model Dev., 13, 3709-3729, https://doi.org/10.5194/gmd-13-3709-2020

Moore, A.M., Arango, H.G., Broquet, G., Edwards, C.A., Veneziani, M., Foley, B.P.D., Doyle, J., Costa, D., Robinson, P., 2011a. The Regional Ocean Modeling System (ROMS) 4-dimensional variational data assimilation systems. Part II: performance and application to the California Current System. *Prog. Oceanogr*. **91**, 50–73.

Moore, A.M., Arango, H.G., Broquet, G., Edwards, C.A., Veneziani, M., Foley, B.P.D., Doyle, J., Costa, D., Robinson, P., 2011b. The Regional Ocean Modeling System (ROMS) 4-dimensional variational data assimilation systems. Part III: observation impact and observation sensitivity in the California Current System. *Prog. Oceanogr.* **91**, 74–94.

Moore, A.M., Edwards, C.A., Fiechter, J., Drake, P., Arango, H.G., Neveu, E., Gürol, S., Weaver, A., 2013. A prototype for an operational regional ocean data assimilation system. In: Xu, Liang, Park, Seon (Eds.), Data Assimilation for Atmospheric, Oceanic and Hydrological Applications, vol. II. Springer, pp. 345–366 (Chapter 14).

Moore, A.M., Jacox, M., Crawford, W., Laughlin, B., Edwards, C., Fiechter, J., 2017. The impact of the ocean observing system on estimates of the California Current circulation spanning three decades. *Prog. Oceanogr*. **156**, 41–60.

Moore, A.M., Edwards, C., Fiechter, J., Jacox, M., 2015. Observing system impacts on estimates of California current transport. In: Liu, Yonggang, Kekering, Heather, Weisberg, Robert (Eds.), Coastal Ocean Observing Systems: Advances and Synthesis. Academic Press, Cambridge, MA, USA, pp. 351–369 (Chapter 19).

Moore, A.M., Martin, M.J., Akella, S., Arango, H.G., Balmaseda, M., Bertino, L., Ciavatta, S., Cornuelle, B., Cummings, J., Frolov, S., Lermusiaux, P., Oddo, P., Oke, P.R., Sorto, A., Teruzzi, A., Vidard, A., Weaver, A.T., 2019. Synthesis of Ocean Observations using Data Assimilation for Operational, Real-time and Reanalysis Systems: A More Complete Picture of the State of the Ocean. *Frontiers in Marine Science* **6:90**. doi:10.3389/fmars.2019.00090.

Mountain, D., 2003. Variability in the properties of Shelf Water in the Middle Atlantic Bight, 1977–1999. *Journal of Geophysical Research*, 108, 3014

Mukai, A.Y., Westerink, J.J., Luettich, R.A., Mark, D., 2002. A tidal constituent database for the western North Atlantic, Gulf of Mexico and Caribbean Sea. *Tech. Rep. ERDC/CHL TR-02-24*, 196pp.

Oke, P.R., Schiller, A., 2007. Impact of Argo, SST, and altimeter data on an eddy resolving ocean reanalysis. *Geophys. Res. Letts*. **34**, L19601. http://dx.doi.org/10.1029/2007GL031549.

Oke, P.R., Sakov, P., 2012. Assessing the footprint of a regional ocean observing system. *J. Mar. Syst*. **105**, 30–51. http://dx.doi.org/10.1016/j.jmarsys.2012.05.009.

Oke, P.R., Larnicol, G., Fujii, Y., Smith, G.C., Lea, D.J., Guinehut, S., Remy, E., Balmaseda, M.A., Rykova, T., Surcel-Colan, D., Martin, M.J., Sellar, A.A., Mulet, S., Turpin, V., 2015a. Assessing the impact of observations on ocean forecasts and reanalyses: Part 1, global studies. *J. Oper. Oceanogr*. 8**,** s49–s62.

Oke, P.R., Larnicol, G., Jones, E.M., Kourafalou, V., Sperrevik, A.K., Carse, F., Tanajura, C.A.S., Mourre, B., Tonani, M., Brassington, G.B., Le Henaff, M., Halliwell, G.R., Atlas, R., Moore, A.M., Edwards, C.A., Martin, M.J., Sellar, A.A., Alvarez, A., De Mey, P., Iskandarani, M., 2015b. Assessing the impact of observations on ocean forecasts and reanalyses: Part 2, regional applications. *J. Oper. Oceanogr*. **8**, s63–s79.

Siedlecki, S. A., Archer, D.E., Mahadevan, A., 2011. Nutrient exchange and ventilation of benthic gases across the continental shelf break. *J. Geophys. Res*., doi:10.1029/2010JC006365.

Simpson, J.H., Bowers, D., 1981. Models of stratification and frontal movement in shelf seas. *Deep Sea Research* **28A**, 727-738.

Smith, G.C., Haines, K. 2009. Evaluation of the S(T) assimilation method with the Argo dataset. *Q. J. R. Meteorol. Soc.*, **135**, 739-756.

Storto, A., Masina, S., Dobricic, S., 2013. Ensemble spread-based assessment of observation impact: application to a global ocean analysis. *Q. J. R. Meteorol. Soc*. **139**, 1842–1862.

Trémolet, Y., 2008. Computation of observation sensitivity and observation impact in incremental variational data assimilation. *Tellus* **60A**, 964–978.

Weaver, A., Courtier, P., 2001. Correlation modelling on the sphere using a generalized diffusion equation. *Quart. J. R. Meteorol. Soc.* **127**, 1815–1846.

Wilkin, J. L., Hunter, E. J., 2013. An assessment of the skill of real-time models of Mid-Atlantic Bight continental shelf circulation, *J. Geophys. Res. Oceans*, **118**, 2919– 2933.

Wilkin, J., Levin, J., Lopez, A., Hunter, E., Zavala-Garay, J., Arango, H., 2018. A Coastal Ocean Forecast System for U.S. Mid-Atlantic Bight and Gulf of Maine. In: Chassignet, E.P., Pascual, A., TintoreÅL, J., Verron, J. (Eds.), New Frontiers in Operational Oceanography, pp. 593–624 (Chapter 21).

Zhang, W., J. Wilkin, O. Schofield, 2010. Simulation of water age and residence time in the New York Bight, *Journal of Physical Oceanography*, **40**, 965-982, doi: 10.1175/2009JPO4249.1.

Zhang, W., Gawarkiewicz, G., 2015. Dynamics of the direct intrusion of Gulf Stream ring water onto the Mid-Atlantic Bight shelf. *Geophys. Res. Lett*. **42**. https://doi.org/10.1002/2015GL065530.